Numerical investigation of droplet-droplet collisions in a water and milk spray with coupled heat and mass transfer

Finotello, Giulia; Padding, Johan T.; Buist, Kay A.; Schijve, Annelien; Jongsma, Alfred; Innings, Fredrik; Kuipers, J.A.M.

Numerical investigation of droplet-droplet collisions in a water and milk spray with coupled heat and mass transfer

Giulia Finotello, Johan T. Padding, Kay A. Buist, Annelien Schijve, Alfred Jongsma, Fredrik Innings & J. A. M. Kuipers

Published online: 20 Aug 2019.

Submit your article to this journal

View related articles

View Crossmark data

Taylor & Francis
Taylor & Francis Group

Numerical investigation of droplet-droplet collisions in a water and milk spray with coupled heat and mass transfer

Giulia Finotello[a], Johan T. Padding[b], Kay A. Buist[a], Annelien Schijve[a], Alfred Jongsma[c], Fredrik Innings[c], and J. A. M. Kuipers[a]

[a]Department of Chemical Engineering and Chemistry, Multiphase Reactors Group, Eindhoven University of Technology, The Netherlands; [b]Department of Process and Energy, Intensified Reaction and Separation Systems, Delft University of Technology, The Netherlands; [c]Tetra Pak CPS, Heerenveen, The Netherlands

ABSTRACT

Large scale simulation models can aid in improving the design of spray dryers. In this work an Eulerian-Lagrangian model with coupled gas phase and droplet heat and mass transfer balances is used to study airflow dynamics, temperature and humidity profiles at different positions in the spray. The turbulent gas flow is solved using large eddy simulation (LES). A turbulent dispersion model accounts for the stochastic subgrid fluid velocity fluctuations along the droplet trajectory. The dispersed phase is treated with Lagrangian transport of droplets, and collisions between droplets which are detected with a stochastic Direct Simulation Monte Carlo (DSMC) method. The outcome of a binary collision is described by collision boundary models for water and milk concentrates. The drying of droplets is modeled by the reaction engineering approach (REA). The effect of the inlet air conditions and of droplet viscosity on the temperature and humidity distributions are analyzed. Most of the heat and mass transfer occurs in the first 10-20 cm from the nozzle where the slip velocities and temperature and humidity driving forces are higher. The droplets size increases, both in the axial and radial direction, because of the dominance of coalescence over separation in the droplet spray studied here. Because the spray domain considered in this work is relatively small, the droplet residence time is small, and consequently the amount of evaporation is still low. The droplet size distributions of milk concentrates are affected by the predominance of coalescence over separation events. The coalescence dominated regime increases when the droplet viscosity is higher.

1. Introduction

Spray dryers are widely used to manufacture powders from liquid feedstock. By evaporating the water of a solution or suspension, the transport weight and volume of a product can be greatly reduced. Spray dryers are used for many applications in food, pharmaceutical industry and in numerous chemical industries. The continuous drying process is controlled to obtain functional powders with desired properties. During the last three decades, spray drying, as an important unit operation, has undergone intensive research and development to produce powders with tailor-made specifications. The powder quality and morphology needs to be optimized towards the desired characteristics of the intended product through control of the atomization, liquid to air flow ratio and collision and drying processes. Coalescence, leading to droplets with larger sizes, and break-up phenomena significantly affect the spray characteristics. Also the physical processes of (coupled) heat and mass transfer, both internal and external to the droplets, strongly influence the drying of the droplets and hence the powder properties. Therefore, extensive knowledge of the heat and mass transfer in the drying droplets and air is desirable for improving the product properties, through a better design and optimization of spray drying process equipment.

Spray drying is an energy intensive operation. The need to reduce energy consumption of spray dryers was addressed by Baker.[1] Applying heat integration

principles is difficult because of the numerous complex process parameters which interact with each other. A correct prediction of the drying process, air temperature and humidity profile in a spray dryer provides crucial data for monitoring the dryer energy consumption, see Goula and Adamopoulos.[2] Process performance improvements are possible if modeling and dryer monitoring are applied. Kim et al.[3] analyzed the effects of various spray drying conditions such as feed solids content, drying temperature, degree of homogenization and initial spray droplet size on the surface composition of spray-dried milk powders under industrial conditions. Their results suggested that a combination of spray drying conditions is necessary to control the surface composition of milk powders.

CFD modeling has widely been used to study simultaneous heat and mass transfer problems in drying processes, see Dlouhy and Gauvin.[4] Fletcher et al.[5] confirmed that proper modeling of the drying behavior of the droplets is essential to ensure a correct quantitative prediction of the droplet behavior in the dryer. In the works of Langrish and Fletcher[6] and Kuriakose and Anandharamakrishnan[7] various examples of applications of computational fluid dynamics in spray drying of food ingredients can be found, predicting the flow patterns and temperature distributions of gas and droplets. Zbicinski et al.[8] and Langrish[9] discussed the different levels and scales of mathematical modeling that can be applied to the spray-drying process. Li and Zbiciński[10] and Zbiciński and Li[11] simulated a cocurrent spray dryer and determined experimentally the initial parameters of the discrete and continuous phases to be used in the model. Accounting for turbulent dispersion and tracking moisture contents in the spray is important for the correct prediction of droplet size distributions.

According to the Reaction Engineering Approach (REA), evaporation of a droplet is an activated process, overcoming an energy barrier, while it is not the case for condensation or adsorption. REA embeds a two-way model, in contrast to the one-way characteristic drying rate curve (CDRC) for predicting single droplet drying. The basis of REA was described by Chen et al.[12] The work of Chen and Putranto[13] provides a comprehensive description of the state-of-the-art of the reaction engineering approach (REA). Chen and Lin[14] compared the REA and CDRC for drying of skim milk and whole milk droplets. The same modeling procedure was used by Qi Lin and Chen[15] to follow the process of single milk droplet drying under elevated humidity conditions by REA. They found that the REA method gave better predictions of the droplet drying than the CDRC method. The REA method was used for modeling whey protein concentrate droplet drying by Patel and Chen[16] and for modeling drying of aqueous lactose droplets by Lin and Chen.[17] The model produced a reasonably good agreement with the experimental data. They concluded that the inlet air temperature, feed temperature and droplet size had a significant impact on the drying rate and the overall product quality.

Huang et al.[18] carried out a computational study on the air flow velocity, temperature and humidity at different axial positions in the spray chamber. Their model was in good agreement with the experimental results of Kieviet and Kerkhof[19] and Kieviet,[20] although the number of comparable measurement points was low because of the considerable difficulties in performing experiments. Droplet-droplet interactions during spray drying were investigated by Mezchericher et al.[21] applying transient calculations. The droplet collisions were found to influence the temperature and humidity patterns while their effect on velocity was less marked. Only droplet coalescence and bouncing were modeled in their work and a complete analysis of the droplet collision outcomes in the spray was missing.

Finotello et al.[22] studied droplet collision outcomes in a spray with a turbulent dispersion model accounting for stochastic subgrid fluid velocity fluctuations along the droplet trajectory. They affirmed that it is important to quantify the frequency of collisions in the spray, as well as the capability to predict the spatial region of the spray where a prevalence of a specific collision regime can be expected. This allows to control the size evolution of the droplets and to optimize the drying process. The prediction of droplet collision outcomes has been the subject of several studies. In these studies four different collision outcomes were found: coalescence, bouncing, reflexive and stretching separation. When two spherical droplets approach each other, a gas layer is formed between the surfaces. If the layer of compressed gas is of such high pressure that the drops are unable to make contact, this results in deformation of both droplets and subsequent bouncing. If the surfaces of the droplets do make contact, coalescence can occur permanently forming one large droplet, or temporarily by reflexive separation or stretching separation. The boundaries between different types of collisions for different fluids and conditions depend on many physical and geometrical parameters.

Our current collision outcome boundary models are based on Ashgriz and Poo[23] and Jiang et al.,[24] with extensions to include viscous dissipation of

energy for highly viscous liquids, see Finotello et al.[25] The model of Jiang et al.[24] showed that the onset of reflexive separation shifts to higher Weber number (We) as the droplet viscosity to surface tension ratio increases. The model was later refined with the introduction of the Ohnesorge (Oh) number by Qian and Law.[26] Brenn and Kolobaric[27] developed a model for the prediction of satellite formation after stretching separation by including the effect of viscosity. The model gave good predictions for highly viscous liquids and high We numbers, but was not able to describe low viscous liquids such as water and alcohol. Ko and Ryou[28] derived equations of mass, momentum and energy to characterize the post-collision parameters of colliding droplets and satellite droplets. Gotaas et al.[29] studied experimentally and numerically the influence of droplet viscosity and observed that the coalescence to separation boundaries shift to higher We number for fluids with higher viscosity. Also Kuschel and Sommerfeld[30] and later Sommerfeld and Kuschel[31] investigated experimentally the effect of viscosity. For the highly viscous liquids they applied a combination of Ashgriz and Poo[23] and Jiang et al.[24] models. The boundary between coalescence and reflexive separation was observed only for small solid mass fractions.

Besides the experiments, there is a growing interest in numerical investigations because these can better elucidate all details of the internal motion of droplets during collision. Viscous dissipation energy profiles and droplet internal flow and stresses are extremely difficult to measure in small scale experiments. Different models for droplet interactions have also been developed from numerical simulation studies, see e.g. Pan and Suga[32] and Munnannur and Reitz[33] and Nikolopoulos et al.[34]

Non-Newtonian droplet collisions occur in spray dryer processes of food products such as powdered milk. Powders are often manufactured from highly viscous liquid suspensions which are non-Newtonian in nature. Few studies are dedicated to non-Newtonian droplet collisions and mostly are based on computational investigations, see Focke and Bothe[35,36] and Sun et al.[37] Only in the work of Finotello et al.,[38] a complete regime map of shear thinning xanthan was obtained. In general, these studies show that the collision dynamics is very complex and strongly dependent on the fluid rheology. Given the complexity of non-Newtonian droplet collisions, for the milk collisions investigated in this work we will use experimentally obtained boundaries between different collision outcomes.[25]

Various experimental studies have been carried out on heat and mass transfer in a spray dryer. Sommerfeld and Qiu[39] measured the mean temperature of a single-phase gas flow in the radial direction at multiple axial positions. Their results showed that for a single-phase flow the temperature of the gas has a radial profile near the gas inlet which flattens at lower downstream position. No measurements were performed for the temperature of the gas in a two-phase flow with droplets. Birchal et al.[40] performed a numerical and experimental study on heat and mass transfer in a spray dryer for milk. Their numerical results showed a radial profile for the air temperature and humidity near the nozzle and a more flattened profile at lower positions in the spray dryer, similar to Sommerfeld and Qiu.[39] Unfortunately, the numerical results for the air temperature were validated with experimental measurements at only one position in the spray dryer. Gianfrancesco et al.[41] studied the development of the air temperature and moisture content in the axial and radial direction for water droplets. Their results showed that most of the drying occurs near the nozzle. They did not find any radial variations in the temperature, in contrast to Birchal et al.,[40] probably due to the low air and liquid flow rates employed in their studies. Despite the different conditions under which these experiments were performed and the different results, there are still similar trends visible. The results of Sommerfeld and Qiu,[39] Birchal et al.[40] and Gianfrancesco et al.[41] all show that most of the drying of the droplets occurs in the region near the droplet atomizer while at lower positions in the spray dryer, there is no or low radial variation in air temperature or moisture content. However, none of these studies presents a complete analysis of the dispersed and continuous phase in presence of heat and mass transfer in terms of size, temperature, moisture distributions and collision frequency. Huang et al.[18] and Gimbun et al.[42] mentioned the lack of carefully obtained experiments due to the challenging operating conditions of high temperature and humidity of the spray dryer and the difficulty of performing detailed measurements.

The main aim of this work is to study the influence of mass and heat transfer between the droplet and gas phase on the distribution and frequency of different types of droplet collision outcomes. Often results on the air flow are decoupled from the dispersed phase, or not shown. Indeed, in all the above-mentioned studies the distribution and frequency of droplet collision events such as coalescence, separation and bouncing were not presented. In this study we start

from our previously developed Euler-Lagrange model[22] based on Direct Simulation Monte Carlo (DSMC), which includes turbulent dispersion of the droplets, and extends it to study droplet behavior in the presence of heat, mass and momentum transfer mechanisms. Moreover, we will conduct a parametric study of the air and droplet phase patterns by varying initial operating conditions in the spray dryer.

The manuscript is organized as follow. In Section 2 the numerical model is described for the dispersed and continuous phase, including the equation for the heat and mass transfer of the gas and droplet phases, a summary of the DSMC method for the detection of droplet collisions and the model to determine the collision outcomes. The operating conditions and geometry of the simulation cases are given in Section 3. The verification of the coupling of the droplet drying model with the gas heat and mass equations is presented in Section 4. The main results are shown and discussed in Section 5. Finally, the conclusions are given in Section 6.

2. Model description

In this study the Euler-Lagrange approach is adopted to model the spray where the detection of droplet collisions is performed with the DSMC method. For an extensive description and validation of the DSMC method, see Pawar et al.[43,44] The gas phase is treated as a continuum and solved on an Eulerian grid where the volume-averaged Navier-Stokes, thermal and species equations are solved, accounting for the momentum, heat and mass exchange between the gas and droplets through source/sink terms. A Lagrangian approach is used for the dispersed phase. A droplet turbulent dispersion model estimates the instantaneous fluid velocity along the droplet trajectory, accounting for subgrid-scale gas velocity which are not resolved in the simulations. For details on the turbulent dispersion model and its effect on droplet-droplet interactions the reader is referred to the work of Finotello et al.[22] The single droplet drying model of the reaction engineering approach is adopted in our work.

2.1. Gas phase mass, momentum, and heat transfer

The heat and mass transfer balances for the gas phase are similar to those previously used in an extended CFD-DEM model of a spout fluidized bed with liquid injection by Sutkar et al.[45] and Van Buijtenen et al.[46]

2.1.1. Mass and momentum equations

The motion of the gas phase is described by the volume-averaged Navier-Stokes equations with conventional two-way coupling for the momentum exchange between the gas phase and the droplets. Both the continuity equation and the momentum equation are solved, see Equations (1) and (2), respectively:

$$\frac{\partial}{\partial t}(\rho_g \varepsilon) + \nabla \cdot (\rho_g \varepsilon \mathbf{u}_g) = 0 \tag{1}$$

$$\frac{\partial}{\partial t}(\rho_g \varepsilon \mathbf{u}_g) + \nabla \cdot (\rho_g \varepsilon \mathbf{u}_g \mathbf{u}_g) = -\varepsilon \nabla P - \nabla \cdot (\varepsilon \bar{\tau}_g) \\ - \mathbf{S}_p + \rho_g \varepsilon \mathbf{g} \tag{2}$$

Here $\mathbf{u}_g$ is the (cell-averaged, filtered) gas velocity, ρ_g the gas density, ε the gas volume fraction (i.e. porosity), P the pressure, and $\bar{\tau}_g$ is the stress tensor. The sink term $\mathbf{S}_p$ is included for the interaction with the discrete droplet phase and is given by:

$$\mathbf{S}_p = \frac{1}{V_{cell}} \int \sum_{i=1}^{N_d} \frac{\beta V_i}{1-\varepsilon} (\mathbf{u}_g - \mathbf{v}_i) \delta(\mathbf{r} - \mathbf{r}_i) dV \tag{3}$$

where V_{cell} is the local volume of the computational cell, V_i the volume of droplet i and $\mathbf{v}_i$ the velocity of droplet i located at r_i. The delta function δ distributes the force acting on the gas phase from the particle or droplet position $\mathbf{r}_i$ to the computational cells $\mathbf{r}$. This term is approximated by using a tri-linear interpolation. The inter-phase momentum transfer coefficient β describes the drag of the gas phase acting on the droplet, which is modeled by a correlation proposed by Beetstra et al.[47] In principle, mass and momentum source terms related to the evaporation should also be included. Because the rate of evaporation is low in the section of the spray considered in this work, we assume that the vapor production does not significantly modify the fluid phase density.

We use the Vreman[48] model to describe the subgrid-scale gas flow effects in Large Eddy Simulations (LES), see also Finotello et al.[22] In LES of turbulent flow, the averaging operator is a linear filtering operator, i.e. a local weighted average over a small volume of fluid. In the averaged Navier-Stokes equations additional terms appear, for which a model has to be assumed before the equations can be solved. The additional terms in the momentum equations are spatial derivatives of the turbulent stress tensor, which are modeled with a subgrid model. The turbulent scales represented by the grid (and larger) are solved explicitly, while the effect of the small subgrid scales is modeled. In LES it is usually assumed that the subgrid turbulent motion is locally homogeneous and isotropic, leading to a relation between subgrid velocity

u_{sgs} and the specific subgrid-scale turbulence kinetic energy k (Irannejad and Jaberi[49] and Sommerfeld[50])

$$u_{sgs} = \sqrt{\frac{2}{3}k} \qquad (4)$$

2.1.2. Heat transfer

The gas phase temperature is obtained by solving the thermal energy equation:

$$\frac{\partial}{\partial t}\left(\varepsilon\rho_g H_g\right) + \nabla \cdot \left(\varepsilon\rho_g \mathbf{u}_g H_g\right) = -\nabla \cdot (\varepsilon\mathbf{q}_h) + S_h \qquad (5)$$

where H_g is the specific enthalpy of the gas, given by the product of the specific heat capacity of the gas at constant pressure and the gas temperature variation:

$$dH_g = C_{p,g} dT_g \qquad (6)$$

where $C_{p,g}$ is the gas specific heat and T_g is the gas temperature. The conductive heat flux $\mathbf{q}_h$ is given by Fourier's law:

$$\mathbf{q}_h = -k_{eff}\nabla T_g \qquad (7)$$

where the effective conductivity k_{eff} is calculated from the pure gas thermal conductivity k_g as:

$$k_{eff} = \frac{1 - \sqrt{1-\varepsilon}}{\varepsilon} k_g \qquad (8)$$

The source term S_h is included for the heat transfer between the droplet and gas phase, and is given by:

$$\mathbf{S}_h = \frac{1}{V_{cell}} \int \sum_{i=1}^{N_d} h_{g,i} A_i \left(T_i - T_g\right) \delta(\mathbf{r} - \mathbf{r}_i) dV \qquad (9)$$

A_i is the surface area of droplet i and T_i its temperature. Note that for our small droplets we assume homogeneous temperature distribution throughout the droplet, as we will briefly discuss in Section 2.2.

In our model, the convective heat transfer coefficient $h_{g,i}$ between droplet i and the gas phase is calculated using the Nusselt correlation given by Ranz and Marshall.[51]

$$Nu = \left[2.0 + 0.6(Re)^{0.5}(Pr)^{0.33}\right] \qquad (10)$$

where the Nusselt number, Reynolds number and Prandtl number are defined as follows:

$$Nu = \frac{h_{g,i} d_i}{k_g}; \quad Re = \frac{\varepsilon\rho_g |\mathbf{u}_g - \mathbf{v}_i| d_i}{\mu_g}; \quad Pr = \frac{\mu_g C_{p,g}}{k_g} \qquad (11)$$

2.1.3. Mass transfer

For the mass transfer of moisture through the gas phase, a similar approach as the heat transfer for the gas phase is used. The moisture mass fraction is obtained by solving the species balance:

$$\frac{\partial}{\partial t}\left(\varepsilon\rho_g w_g\right) + \nabla \cdot \left(\varepsilon\rho_g \mathbf{u}_g w_g\right) = -\nabla \cdot (\varepsilon\rho_g \mathbf{q}_m) + S_m \qquad (12)$$

where w_g is the mass fraction of moisture in the gas phase. The conductive mass transfer flux $\mathbf{q}_m$ is given by Fick's law:

$$\mathbf{q}_m = -D_{eff,g}\nabla w_g \qquad (13)$$

where the effective moisture diffusivity $D_{eff,g}$ is calculated from the moisture diffusivity in a pure gas (without droplets) $D_{e,g}$ and gas volume fraction ε as:

$$D_{eff,g} = \frac{1 - \sqrt{1-\varepsilon}}{\varepsilon} D_{e,g} \qquad (14)$$

The source term S_m is included for the mass transfer between the droplet and gas phase, and is given by:

$$\mathbf{S}_m = \frac{1}{V_{cell}} \int \sum_{i=1}^{N_d} k_{m,i} A_i \rho_g \left(w_{g,i}^* - w_g\right) \delta(\mathbf{r} - \mathbf{r}_i) dV \qquad (15)$$

where $w_{g,i}^*$ is the partial vapor content at the surface of the droplet i, to be discussed in Section 2.2.2. The mass transfer coefficient $k_{m,i}$ between droplet i and the gas phase is calculated using the empirical Sherwood correlation given by Ranz and Marshall:[51]

$$Sh = \left[2.0 + 0.6(Re)^{0.5}(Sc)^{0.33}\right] \qquad (16)$$

where the Sherwood number and Schmidt number are defined as follows:

$$Sh = \frac{k_{m,i} d_i}{D_{e,g}}; \quad Sc = \frac{\mu_g}{\rho_g D_{e,g}} \qquad (17)$$

2.2. Droplet phase heat, mass and momentum transfer

The drying of droplets is characterized by simultaneous heat, mass and momentum transfer. During the drying process, moisture is evaporating from the droplet surface. This will cause the droplet diameter to decrease. In the model, the droplets are assumed to remain spherical, homogeneous in composition and with a uniform temperature inside the droplets (Biot number, $Bi < 0.1$, Sutkar et al.[45]). This approximation is valid for sufficiently small liquid droplets.

2.2.1. Droplet dynamics and turbulent dispersion

In the Lagrangian approach, the equations of motion of each droplet are given by:

$$\frac{d\mathbf{r}_i}{dt} = \mathbf{v}_i \qquad (18)$$

$$\frac{d\mathbf{v}_i}{dt} = \frac{\mathbf{u}_{rel}}{\tau_d} - \frac{\nabla p}{\rho_p} + \mathbf{g} \qquad (19)$$

where the droplet dynamic relaxation time is:

$$\tau_d = \frac{d_i^2 \rho_l}{18\mu_g f(Re)} \qquad (20)$$

and $\mathbf{u}_{rel} = \mathbf{u}_g - \mathbf{v}_i$ is the local relative velocity between the droplet and gas phase. The latter is given by $\mathbf{u}_g = \bar{\mathbf{u}}_g + \mathbf{u}_d^*$. $\mathbf{u}_g$ is the gas velocity at the location of droplet i, $\bar{\mathbf{u}}_g$ is the filtered resolved velocity and $\mathbf{u}_d^*$ the stochastic subgrid velocity at the location of droplet i. $f(Re)$ is the drag factor.[47] The subgrid velocity is modeled by a Langevin equation, and is updated according to:

$$\mathbf{u}^{*n+1} = \left(1 - \frac{\Delta t}{\tau_L^*}\right)\mathbf{u}^{*n} + u_{sgs}\sqrt{\frac{2\Delta t}{\tau_L^*}}\zeta \qquad (21)$$

with u_{sgs} given by Equation (4) and τ_L^* the Lagrangian time scale, given by:

$$\tau_L^* = \frac{\tau_{sgs}}{\sqrt{1 + \vartheta^2}} \qquad (22)$$

Here $\tau_{sgs} = C_{sgs}\bar{\Delta}/u_{sgs}$ is the characteristic subgrid time scale and $\vartheta = |\bar{\mathbf{u}} - \mathbf{v}_i|/u_{sgs}$ is the normalized drift velocity. C_{sgs} is an empirical constant equal to 0.1 and $\bar{\Delta}$ is the filter width.[52] The random vector ζ is obtained from a isotropic 3 D Gaussian distribution with mean 0 and standard deviation (in each Cartesian direction) of 1. In case $\Delta t > \tau_L^*$ the new residual velocity is directly obtained from $\mathbf{u}^* = u_{sgs}\zeta$.

2.2.2. Droplet heat and mass transfer
The heat and mass balance for the droplets are described by Equations (23) and (24), respectively.

$$H_{f,g}\dot{m}_i + m_i C_{p,i}\frac{dT_i}{dt} = h_{g,i}A_i(T_g - T_i) \qquad (23)$$

$H_{f,g}$ is the specific latent heat of evaporation, m_i is the mass of droplet i and $\dot{m}_i$ the rate of liquid evaporation from the droplet surface, determined as:

$$\dot{m}_i = \frac{dm_i}{dt} = -k_{m,i}A_i\rho_g\left(w_{g,i}^* - w_g\right) \qquad (24)$$

$\dot{m}$ is generally negative, because water is evaporating from the surface.

The partial vapor content at the droplet surface $w_{g,i}^*$ can be obtained from the partial vapor pressure at the droplet surface:

$$w_{g,i}^* = \frac{P_{v,i}^* M_d}{PM_{air}} \qquad (25)$$

where M_d is the molecular weight of the liquid in the droplet, M_{air} is the molecular weight of air and P is the ambient pressure. The partial vapor pressure at the droplet surface is determined by using the Clausius-Clapeyron equation, with R the ideal gas constant:

$$\ln\left(\frac{P_{v,i}^*(T_i)}{P_v^*(T_{ref})}\right) = \frac{H_{f,g}}{R}\left(\frac{1}{T_{ref}} - \frac{1}{T_i}\right) \qquad (26)$$

The partial vapor content at the surface of a droplet containing dissolved solids is calculated with a fractionality, $w_{g,i}^* = \Psi_i\frac{P_{v,i}^* M_d}{PM_{air}}$. An Arrhenius equation is used to calculate the fractionality Ψ:

$$\Psi_i = \exp\left[-\frac{\Delta E_{v,i}}{RT_i}\right] \qquad (27)$$

$\Delta E_{v,i}$ is the apparent activation energy that represents the driving force to remove moisture from the droplet during drying. For whole milk, Chen and Lin:[14]

$$\frac{\Delta E_{v,i}}{\Delta E_{v,g}} = 0.957\exp\left[-1.291(X_i - X_g)^{0.934}\right] \qquad (28)$$

where X_i is the wet fraction of the particle and X_g is the moisture content corresponding to the bulk condition of the air phase. The apparent activation energy $\Delta E_{v,g}$ is expressed by:

$$\Delta E_{v,g} = -RT\ln(RH_g) \qquad (29)$$

where $RH_g = P_v(T_{g,\infty})/P_{v,sat}^*(T_g)$ is the relative humidity assuming that the drying agent is an ideal gas. $P_v(T_{g,\infty})$ is the partial vapor pressure in the bulk of the gas phase and $P_{v,sat}^*(T_g)$ is the saturation vapor pressure.

2.2.3. Collision detection and collision outcome
We present the main features of the adapted DSMC method used in this work. For details the reader is referred to Pawar et al.[43] With this approach, a group of droplets, a parcel, is represented by a single droplet. Only the trajectories of these representative droplets need to be calculated.

The region within which a droplet of diameter d_i searches its collision partners is a local spherical searching scope of radius $R_{s,i}$. An important feature of the adapted DSMC method is that the size of the searching scope is dynamically adapted, such that a sufficiently large neighborhood of the droplet is scanned for possible collision partners, *independent* of the chosen CFD cell size (in contrast to the other DSMC approaches). The collision frequency is:

$$f_i = \sum_{j\in R_{s,i}}|v_{i,j}|\frac{\pi}{4}(d_i + d_j)^2\frac{n_j}{\frac{4}{3}\pi R_{s,i}^3} \qquad (30)$$

where j indicates a droplet within the searching scope of the droplet i, $|v_{ij}|$ is the magnitude of the relative velocity, $\frac{\pi}{4}(d_i + d_j)^2$ is the effective collision area, $\frac{4}{3}\pi R_{s,i}^3$ the volume of the searching scope and n_j the real number of droplets represented by the parcel j, or parcel size. During one droplet time step $\Delta t_{d,i}$, the probability of droplet collision should be less than 1 because inter-droplet collisions need to be distinguished from free droplet motion. To achieve this, the droplet time step is adjusted, depending on the mean free path of each moving droplet, $L_i = |v_i|/f_i$. The droplet time step is limited by the gas time step Δt_g, and therefore given by $\Delta t_{d,i} = \min\left[\frac{L_i}{3v_i}, \Delta t_g\right]$.

The collision probability between a specific pair of droplets i and j is:

$$P_{ij} = |v_{i,j}|\frac{\pi}{4}(d_i + d_j)^2 \frac{n_j \Delta t_{d,i}}{\frac{4}{3}\pi R_{s,i}^3} \qquad (31)$$

A collision occurs only if $\chi > \frac{j}{N_i} - P_{ij}$ where χ is a random number with uniform distribution between 0 and 1, j is the candidate collision partner chosen as $j = \text{int}[\chi N_i] + 1$ and N_i is the total number of droplets in the searching scope of i.

Once a collision pair is detected, the outcome of the binary collision needs to be predicted. Phenomenological models for the collision outcome are usually expressed in terms of Weber number, Ohnesorge number, impact parameter and size ratio:

$$We = \frac{\rho_d d_s |v_{ij}|^2}{\sigma}; \quad Oh = \frac{\mu_d}{\sqrt{\rho_d d_s \sigma}}; \quad B = \frac{2b}{d_s + d_l};$$

$$\Delta = \frac{d_s}{d_l}$$

$$(32)$$

where ρ_d is the droplet density, d_s and d_l are the diameters of the smallest and largest droplet in the pair, respectively. σ is the surface tension and μ_d is the droplet fluid viscosity. The Weber number is the ratio between inertia forces and surface tension. To account for viscosity the Ohnesorge number is used, which represents the ratio of viscous forces and the combined effect of inertial forces and surface tension. The impact parameter **B** is defined, before the moment of impact, as the distance **b** between the two droplet centers in the plane perpendicular to the relative velocity vector, normalized by the average droplet diameter. When **B** is equal to 0 we are dealing with a head-on collision and when it is 1 a grazing collision.

The impact parameter, however, is not a deterministic parameter for each specific collision, since the DSMC simulation does not specifically track the trajectories of all individual droplets. Therefore, it is assumed that droplets collide at random positions with a normalized probability distribution given by $P(B) = \sqrt{\xi}$, with ξ a uniform random number between 0 and 1. This probability distribution accounts for the fact that lower impact parameters have less probability than high impact parameters. For water spray the boundary collision model of Ashgriz and Poo[23] is applied. The bouncing regime is predicted by the model of Estrade et al.[53] For milk concentrates and the reference fluid we use the model by Finotello et al.[25] expressed as:

$$We_{reflexive} = 3\left[7(1 + \Delta^3)^{2/3} - 4(1 + \Delta^2)\right]\frac{\Delta(1 + \Delta^3)^2}{(\Delta^6 \eta_1 + \eta_2)}$$
$$+ W_{translation}$$

$$(33)$$

$$We_{translation} = We_{milk,crit} - We_{water,crit} \qquad (34)$$

$$We_{milk,crit} = 17.05 + 510 \cdot Oh \qquad (35)$$

Here η_1 and η_2 are geometric factors as introduced by Ashgriz and Poo.[23]

$$We_{stretching} = \left[\frac{3.0}{B}\left(1 + 0.05\frac{\mu}{\sigma}\sqrt{\frac{\rho d}{\sigma}}\right)\right]^2 \qquad (36)$$

In case of coalescence, the smallest droplet is removed from the simulation and the size of the larger droplet is updated, based on conservation of mass. In case of reflexive separation and stretching separation, one or more new (satellite) droplets can be generated. Consequently, the mass and volume of the parent droplets is reduced. A model predicting the number and size of the satellite droplets was adapted from Ko et al.[28] In all cases, a momentum balance is used to calculate the new velocities after collision.

In this study, milk droplet collisions are simplified in the sense that only droplet-droplet interactions are considered. In reality, during drying the viscosity of the milk droplets increases due to evaporation of the water content. Partially wet particles are formed and a sticky point, dependent on the temperature and moisture content of the particle, can be reached. Between the high viscosity/high surface tension state and the solid glassy non-sticky state there is a sticky region. If the temperature and the residual moisture content of the particle resides in the sticky region, the partially dried droplets, which by now are better described as particles, are prone to stick. Collisions and consequent adhesions of such sticky particles generate agglomerates of primary particles. Verdurmen et al.[54] classified all the colliding droplets and particles in the spray depending on their viscosity and temperature of the sticky point. Sommerfeld and Stübing[55]

considered the agglomeration efficiency based on the kinetic, dissipated and van der Waals energies of the particles. Because the available models of agglomeration are limited by the high complexity of particle-air interactions in a spray dryer, we decided to not include yet an agglomeration model. Moreover in the spray system considered in this work only around 2% of the droplets, calculated over the total number of collisions, reaches the sticky point temperature and therefore are prone to agglomerate.

3. Numerical simulation geometry and parameters

In Table 1, the physical properties of the liquids used in this work for investigating the effect of viscosity are reported.

In our spray dryer model, a nozzle is placed 20 cm from the top of a rectangular domain. For the domain boundary conditions a prescribed pressure, temperature and humidity is used. The boundaries allow for inflow and outflow of gas. The gas flow is introduced continuously from the entire top boundary with inlet velocity generated according to a Gaussian distribution with $v_{max} = 25$ m/s and variance $= Lx/2$, where Lx is the domain width. Droplets are immediately eliminated when the system boundaries are crossed. In the Lagrangian method a single particle in the simulation is representative of a large number of real particles in the spray. In this work a simulated droplet is representative of 1500 droplets. We checked the effect of grid size and parcel number on the droplet size distribution. The results remain essentially the same for a refined grid size of $80 \times 80 \times 140$ and for a parcel number of 2500.

In the numerical spray model, new droplets are introduced from a hollow cylinder with outer diameter $d_{out} = d_{in} + 2\delta_l$, where d_{in} is the inner diameter and δ_l the liquid sheet thickness. Droplets are assumed to be spherical and released with an angle direction linearly proportional to the radial position so that the axial and radial velocities are: $v_{zi} = v_{inj} \cos(2r_i\theta/d_{out})$ and $v_{ri} = v_{inj} \sin(2r_i\theta/d_{out})$, where v_{inj} is the initial nozzle injection velocity, d_{out} is the outer cone diameter, θ is the spray cone angle and r_i is the radial position of the drop from the symmetry

axis of the spray. For many real sprays, the Rosin-Rammler distribution closely predicts the droplet size distribution. According to this distribution, the mass fraction of all droplets with a diameter smaller than d, $Y(d)$, is equal to:

$$1 - Y(d) = \exp\left[-\left(\frac{d}{\bar{d}}\right)^{n_s}\right] \qquad (37)$$

where $\bar{d}$ is the Rosin-Rammler diameter and n_s is the spreading parameter. New droplets are introduced in a cylindrical region until the introduced cumulative mass is equal to the desired total mass for the given time step. Droplet diameters are generated in accordance with Equation (37) by generating a uniform random number ξ between 0 and 1 and then choosing $d = \bar{d}(-\ln\xi)^{\frac{1}{n_s}}$. The smallest droplets whose collective masses amount 0.5% of the total injected mass as well as the biggest droplets with a collective mass of 0.5% of the total mass are excluded. Additionally, another random number is generated, which has to be smaller than $(d_{0.5\%}/d)^3$ for the droplet to be accepted for insertion into the system. The reason for this additional step is that the *number* of droplets in a given size interval of the Rosin-Rammler distribution, which is itself a cumulative *mass* probability, scales with d^{-3}.

If a droplet in the spray dryer domain evaporates completely, it is eliminated (the excluded droplets have a collective mass which is smaller than the 0.1% of the total mass in the spray). Droplet temperature and diameter are calculated by assuming a perfect mixing model with specific heat capacity C_p, thermal conductivity k_g and heat transfer coefficient h_g not depending on temperature and humidity variations.

In Table 2, the parameters for simulations are given. The changes of inlet conditions of all simulations are shown in Table 3.

4. Model verification

4.1. Heat and mass transfer coupling test

The following simulation is performed to test the coupling between the heat and mass transfer. For this test case, a droplet with a temperature of 300 K was placed in the middle of a domain of $0.2 \times 0.2 \times 0.6$ m. The size and moisture content of the droplet were set at a

Table 1. Physical properties of the liquids.

Liquids	Droplets density [kg/m³]	Droplets viscosity [Pas]	Droplets surface tension [N/m]
Water	1000	0.001	$73 \times \cdot 10^{-3}$
Milk 20% TS	1041	0.0043	$46.8 \times \cdot 10^{-3}$
Milk 46% TS	1094	0.083	$46.9 \times \cdot 10^{-3}$
Reference fluid	1094	1.2	$48 \times \cdot 10^{-3}$

Table 2. Simulation parameters.

Parameters	Symbols	Values
Number of Eulerian cells	$NX \times NY \times NZ$	$60 \times 60 \times 120$
System width [m]	Lx	0.6
System depth [m]	Ly	0.6
System height [m]	Lz	1.2
Mass flow rate [kg/s]	q	0.1275
Nozzle radius [m]	d_{in}	0.889×10^{-3}
Rosin-Rammler spreading parameter	n	3.5
Inlet droplets velocity [m/s]	v_{inj}	200
Initial Sauter mean droplet radius [m]	r_{mean}	25.5×10^{-6}
Cone nozzle spray angle [degree]	θ	81
Gas inlet temperature [K]	$T_{g,in}$	353
Droplets inlet temperature [K]	$T_{d,in}$	296.65
Gas inlet moisture content [kg/kg]	w_g	0.01
Parcel size	n_i	1500
Typical number of droplets in the system		10^9

Table 3. Parameters of the simulations of this work.

Simulations	Liquid flow rate [kg/s]	Gas inlet temperature [K]	Gas inlet moisture content [kg/kg]
Test cases on water			
Without drying and without coupling	0.275	353.15	0.01
With drying and without coupling			
With drying and with coupling			
Parametric study on water			
Liquid flow rate test	**A** 0.275	433.15	0.01
	B 0.175		
	C 0.375		
Inlet gas temperature test	0.275	**A** 433.15	0.01
		D 393.15	
		E 473.15	
Inlet gas moisture content test	0.275	433.15	**A** 0.01
			F 0.001
			G 0.1
Viscosity influence			
Milk 20% TS	0.275	433.15	0.01
Milk 46% TS			
Reference fluid			

Table 4. Simulation settings for the single droplet test.

Parameter	Value
Domain dimensions	$0.2 \times 0.2 \times 0.6$ m
Grid cells	$22 \times 22 \times 34$
Timestep flowsolver	$2.5 \cdot \times 10^{-6}$ s
Diffusion coefficient	21.2×10^{-6} m²/s
Gas temperature	300 K
Gas velocity	0.45 m·s^{-1}
Droplet inlet temperature	300 K
Sauter mean droplet radius	1.00×10^{-3} m

constant value. The gas flowing into the domain had a temperature of 300 K and a velocity of 0.45 m/s. An overview of the used simulation settings can be found in Table 4. As a hot gas flow passes around a droplet, the droplet will evaporate and the temperature of the droplet will decrease until it reaches the wet-bulb temperature.

In Figure 1, the domain with the single droplet is shown at different time steps. It can be seen that the temperature of the droplet decreases very fast while the temperature of the gas behind the droplet decreases slightly.

In Figure 2, the temperature of the droplet and the theoretical wet bulb temperature for a relative humidity of 0.3, 0.5, and 0.7 are shown. The theoretical wet bulb temperature is calculated, using the dry-bulb temperature, the relative humidity and the pressure, see.[56] For all three different relative humidities, after a certain time the droplets reach the wet bulb temperature as expected. From these results we conclude that the coupling between the heat and mass transfer for the droplets was included properly.

4.2. Gas-liquid mass transfer test

For the verification of the convective mass transfer between the gas phase and the liquid phase, a test case with a fixed bed of droplets was conducted. In the fixed bed, the initial moisture mass fraction of the gas phase was equal to 0.005 and the one of the inlet gas was set 100 times higher, at 0.5. Four simulations with a different inlet gas velocity of 0.25 m/s, 0.5 m/s, 0.75 m/s, and 1.0 m/s were performed. The temperature of the gas phase and the droplets was set to 353 K and was kept constant during the simulation. After a transient state a steady moisture mass fraction profile was developed in the bed. The results were

compared with an analytical solution obtained from a one-dimensional heterogeneous plug flow model, given by:

$$\frac{<w_g>}{<w_{g,0}>} = \exp\left(\frac{-k_m a_d z}{u_z}\right) \qquad (38)$$

In this model, the axial dispersion in the gas phase is neglected. The simulation settings that were used for this case are given in Table 5.

In Figure 3, the steady state simulation and analytical results of this test case are shown for the four different velocities. The simulation results are in good agreement with the analytical solution for all four velocities. These results indicate a correct coupling between the gas phase and the liquid phase.

5. Results and discussion

When droplets are sprayed in the domain they contact hot air flow at low humidity. Because of the differences in temperature and moisture mass fraction, heat and mass transfer occurs between the gas and droplets. The difference in vapor pressure of the droplet and the ambient pressure of the vapor far from the droplets in the gas phase drives mass transfer from the liquid to the gas phase. This mass flux leads to the evaporation of the liquid and to the increase of the relative humidity in the gas phase. Due to the evaporation of water, the temperature of the droplet will initially decrease. The associated transferred energy is the enthalpy of vaporization. Then when the rate of evaporation decreases the droplet temperature will increase. The rate of evaporation depends on the rate of vapor removal from the liquid surface by diffusion and convection. Simultaneously, the necessary heat required for evaporation of the liquid must be supplied to the droplets by heat conduction and convection from the gas phase. As a result, the temperature of the gas will decrease. Under equilibrium conditions the temperature of the surface of the droplets and hence the vapor pressure at the surface will be such that the heat transfer and mass transfer rates are balanced.

Figure 1. Snapshots of the cross-section of the domain in the length and width at $t = 0$ s, $t = 0.04$ s and $t = 0.08$ s.

Table 5. Simulation settings for the fixed bed test.

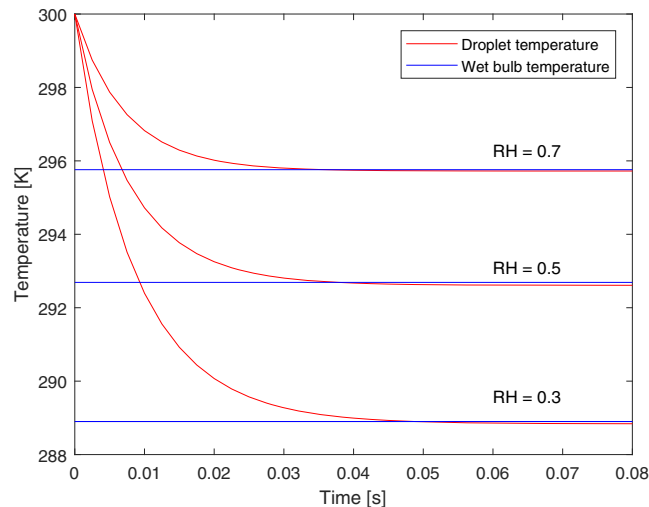| Parameter	Value
Domain dimensions	$0.02 \times 0.02 \times 0.2$ m
Grid cells	$8 \times 8 \times 40$
Timestep flowsolver	$2.5 \times 10^{-6} s$
Number of particles	$48 \times 48 \times 480$
Diffusion coefficient	21.2×10^{-6} m^2/s
Gas temperature	353 K
Gas velocity	0.25/0.5/0.75/1 m/s
Droplet inlet temperature	353 K
Sauter mean droplet radius	25.5×10^{-6} m
Initial moisture mass fraction	0.005
Inlet moisture mass fraction	0.5

Figure 2. Wet bulb temperature for a relative humidity of 0.3, 0.5, and 0.7.

5.1. Effect of the drying and heat and mass transfer

Our previous work,[22] revealed that the inclusion of droplet interactions and a turbulent dispersion model strongly influence the size distribution along the spray as well as the rate of collisions. We will now investigate the influence of droplet drying, and the incorporation of two-way coupling of heat and mass transfer between droplet and gas, on the droplet spray characteristics. To this end we first run a nondrying spray system in a steady state, after which we suddenly switched on the drying (with or without two-way coupling), see the settings for test cases on water in Table 3. Figure 4(a) shows that, as expected, the average diameter of all the droplets in the spray system

remains constant if drying and coupling are neglected, but is lower if the drying is considered. Without coupling the driving force for the drying is larger because the gas temperature and humidity maintain constant values. With two-way coupling, the temperature of the gas is lower, and the moisture content of the gas is higher, in the vicinity of the droplet than in the bulk. Figure 4(b) shows a higher average temperature with two-way coupling than without. In the spray droplets heat up because of the hot air but at the same time their temperature decreases because of evaporation. Without coupling more latent heat is removed from the droplet leading to a lower temperature of the droplet. The average droplet size and temperature in the simulation domain reach a steady state in less
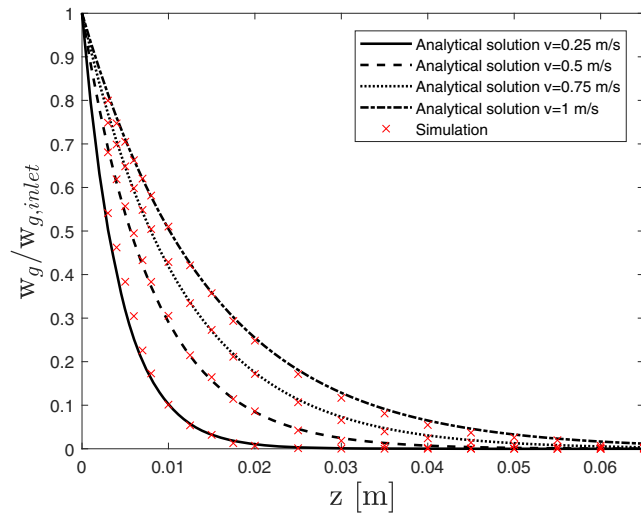

Figure 3. Computed concentration profiles and analytical solution for $v = 0.25$ m/s, $v = 0.5$ m/s, $v = 0.75$ m/s and $v = 1$ m/s (symbols indicate the simulation results; lines indicate the analytical solution).
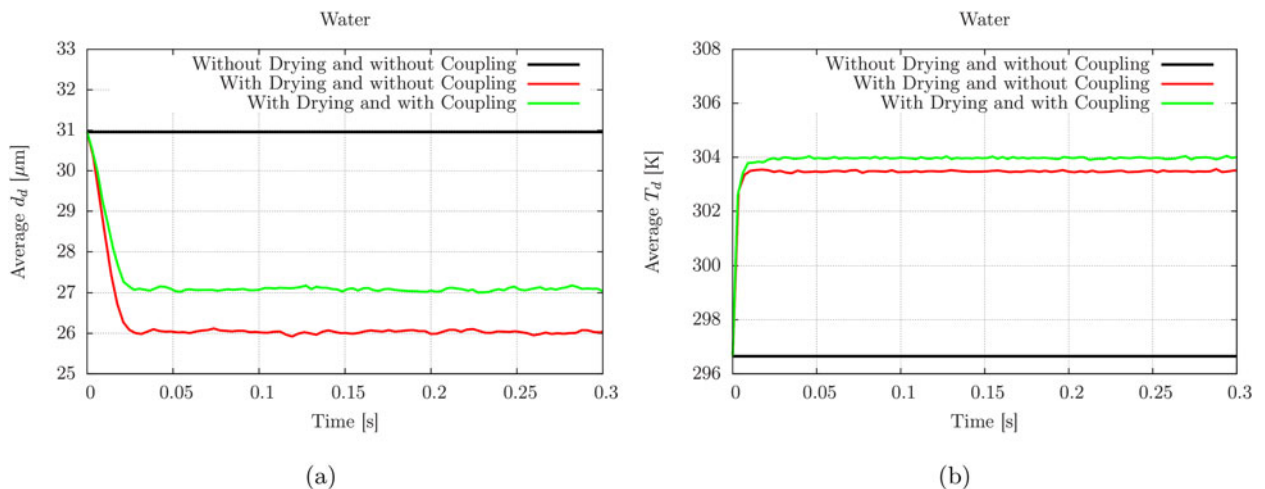

Figure 4. Data from simulations in presence or absence of the droplet drying and heat and mass transfer coupling, respectively. Average diameter (a), average temperature (b) of all the drops in the spray domain versus the simulation time.
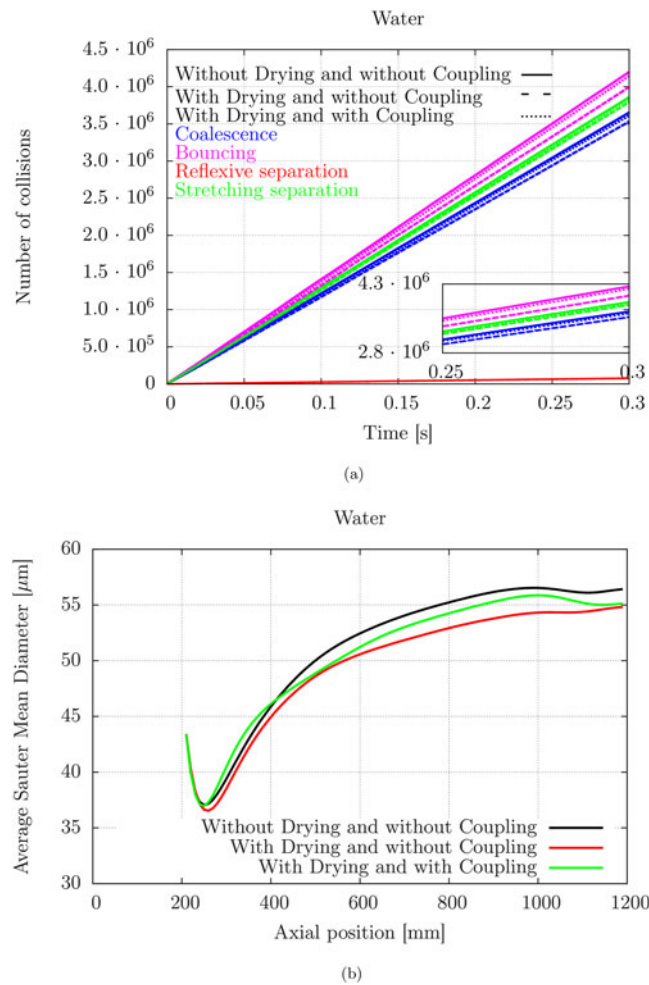
Figure 5. Data from simulations in presence or absence of the droplet drying and heat and mass transfer coupling, respectively. Cumulative number of collisions (a) of the drops in the spray system over the total time and Sauter mean diameter (b) averaged in the lateral direction as a function of the axial position.

than 50 ms. This is in agreement with the relatively short residence time of the droplets in our domain, caused by the high droplet inlet velocity.

Because the droplet diameters decrease, a lower rate of droplet collisions is expected, as well as a decrease of the Sauter Mean Diameter (SMD). Indeed Figure 5(a) shows a slight reduction of the number of collisions. In Figure 5(b), the Sauter Mean Diameter is larger when the axial distance from the droplet inlet is larger. This is caused by coalescence of droplets. When including drying and coupling, the SMD at each axial positions is slightly lower. We note here that the effects are not very large because of the relatively short residence time of the droplets in the system.

5.2. Parametric study on water with variation of inlet conditions

The variation of inlet conditions of the air and droplets enables us to evaluate the influence of the drying kinetics on the spray dryer performance. The inlet liquid flow rate, the inlet gas temperature and moisture content are changed and the relative effects are investigated in terms of temperature and moisture content of the gas, temperature of the droplets and evaporated fraction.

5.2.1. Liquid flow rate
In Figure 6, three different liquid flow rates are used, maintaining the same operating conditions, and showing the radial profiles of temperature of the gas T_g, moisture content of the gas w_g, average temperature of the droplet T_{drop} and evaporated volume from the droplet phase to the air phase per unit time. The variation of the air flow patterns is confined to the central region of the spray dryer where the droplet spray is developed while the remaining volume of the domain has constant air temperature and humidity. When increasing the inlet liquid flow rate Q, a larger liquid mass is introduced in the spray, and therefore more
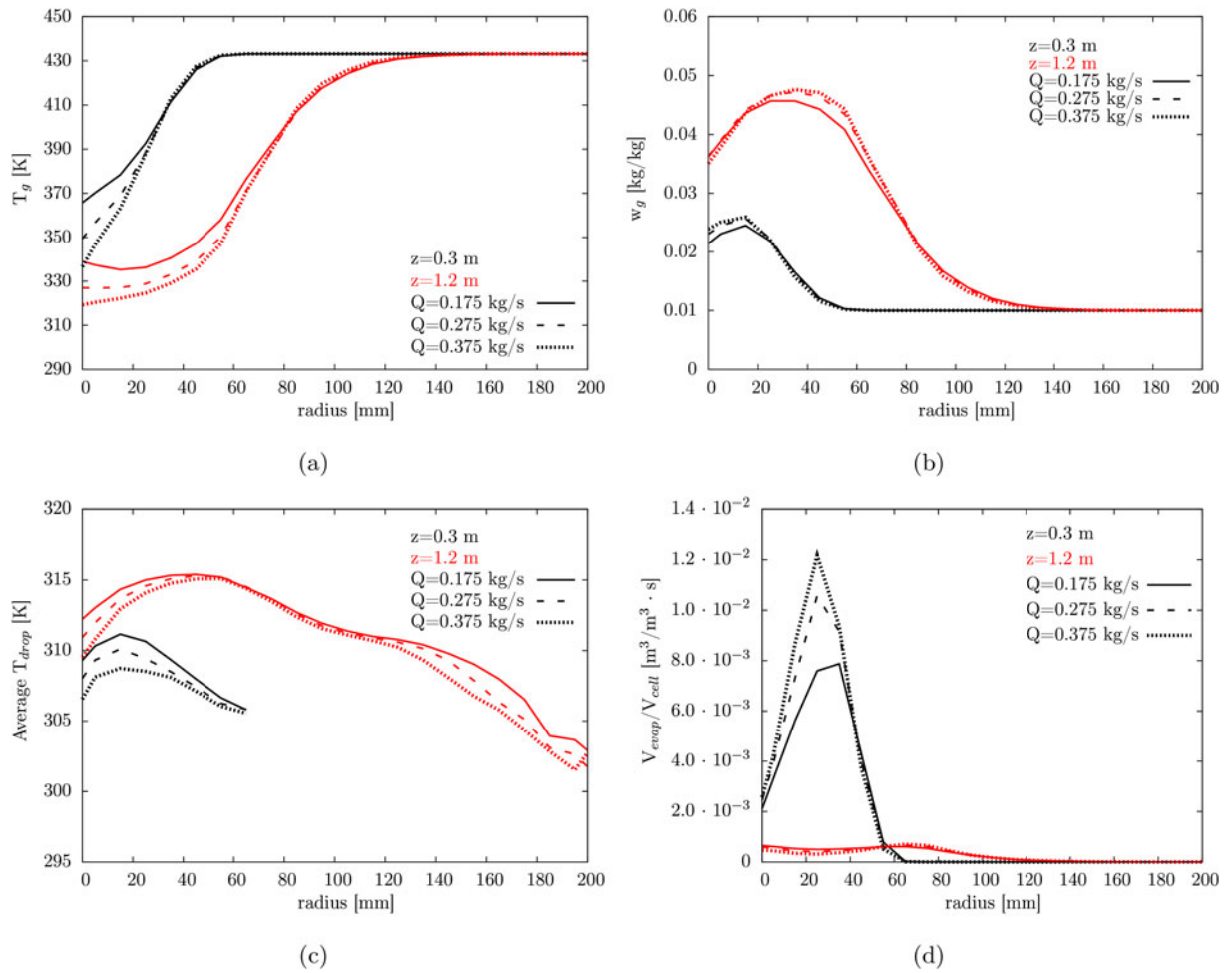
Figure 6. Temperature of the gas T_g (a), moisture content of the gas w_g (b), average temperature of the droplet T_{drop} (c) and normalized evaporated volume from the droplet phase to the air phase V_{evap}/V_{cell} per unit time (d) in the lateral direction at two axial distances from the nozzle and for different liquid flow rates.

heat and mass transfer can occur. In the region close to the inlet of the droplets ($T_{drop,in} = 296.65$ K), their temperature rises rapidly because of the large difference with the temperature of the surrounding air. The rate of temperature rise slows down at larger axial distance from the nozzle. If the liquid flow rate is lower, the temperature driving force is larger thus the average T_{drop} can locally increase. In Figures 6–8, the profiles are shown from 0 to 200 mm and not from 0 to 300 mm since the temperature, moisture content and evaporated volume remain constant after 200 mm. The profiles for the droplet parameters are not shown beyond 200 mm because no droplets are present from 200 to 300 mm.

Figure 9 provides useful information about the droplet collision behavior in the spray dryer. Coalescence occurs in a wider volume of the spray while reflexive separation is limited to the proximity of the symmetry axis where the droplet velocities are higher. Most collisions occur in a more or less tubular

region at higher axial distances and in the initial spray angle. In this initial region the effect of the large axial and lateral velocities is larger than at larger axial distances, so the We numbers are larger. This explains the dominance of separation events in the initial spray close to the nozzle.

The temperature of the droplets approaches the temperature of the surrounding air at an axial distance $z = 1.2$ m but the minimum $\Delta T = T_g - T_{drop} \sim 25$K is still high meaning that the evaporation is not complete. For a domain longer than 1 m, and thus a longer residence time of the droplets, the remaining driving force can be used for further evaporation. Figure 6(d) confirms that the highest rate of evaporation of water droplets occurs in the proximity of the spray inlet. The core region of the spray is characterized by less evaporation at $z = 0.3$ m because the droplets are introduced with a hollow cone configuration, therefore less droplets are present close to the central axis. The edges of the spray are continuously
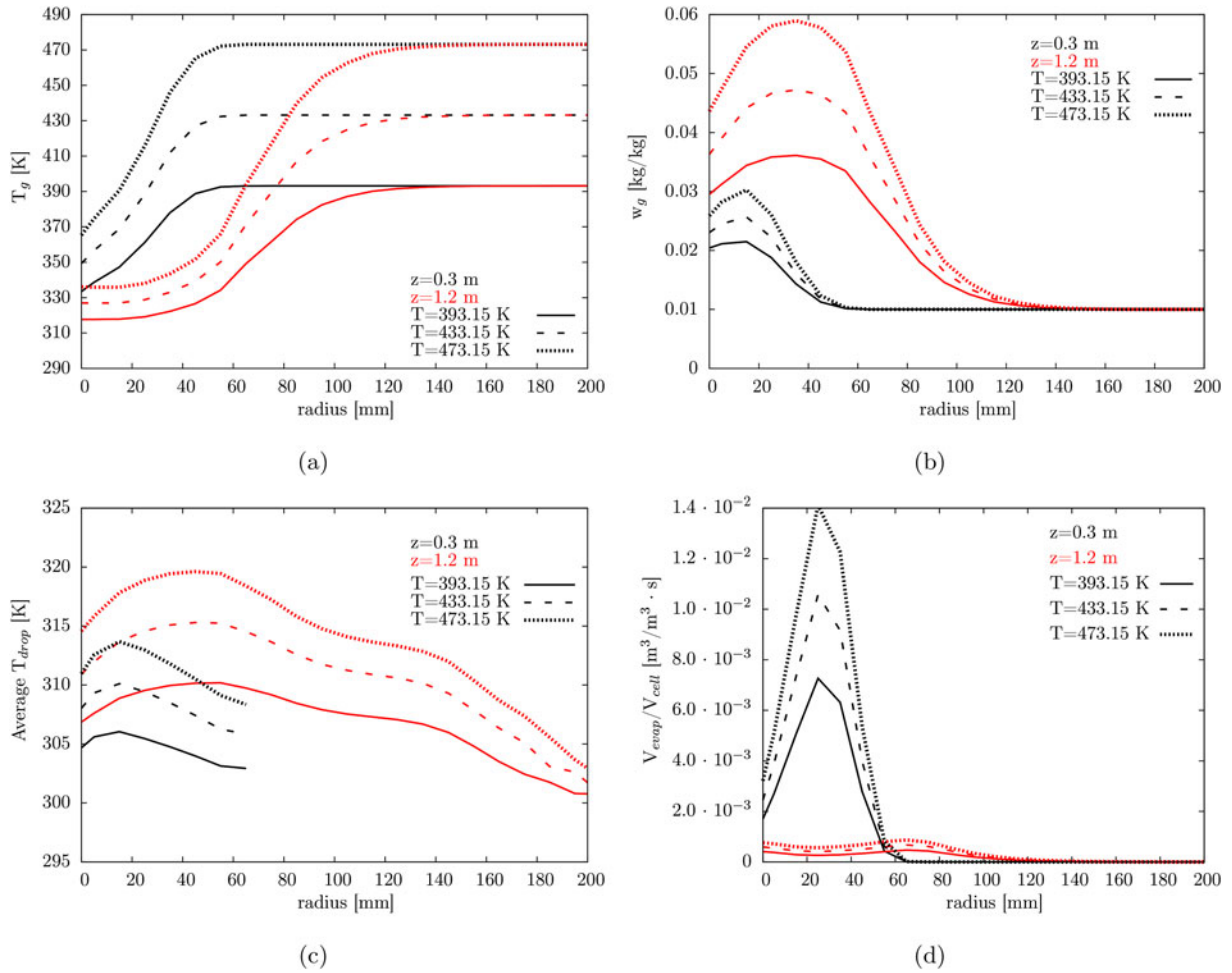
Figure 7. Temperature of the gas T_g (a), moisture content of the gas w_g (b), average temperature of the droplet T_{drop} (c) and normalized evaporated volume from the droplet phase to the air phase V_{evap}/V_{cell} per unit time (d) in the radial direction at two axial distances from the nozzle and for different inlet air temperatures.

diluted with the air which is still at inlet conditions while in the core of the spray the air becomes saturated due to evaporation. The spray performance depends on the combined effect of air mixing which favors heat and mass transfer or air entrainment which maintains saturation conditions.

5.2.2. Inlet gas temperature

Figure 7 shows the radial profiles of temperature of the gas T_g, moisture content of the gas w_g, average temperature of the droplet T_{drop} and evaporated volume of vapor from the droplets to the air per unit time for three different values of inlet air temperature. As expected, more water is evaporated from the droplets at higher $T_{g,in}$. Therefore, with increasing the inlet air temperature $T_{g,in}$, the drying process has an higher intensity. This can be observed also by the temperature difference for a fixed lateral position $T_{g,r}(z=0.3$ m$)$-$T_{g,r}(z=1.2$ m$)$ or by the vapor content in the air $w_{g,r}(z=1.2$ m$)$-$w_{g,r}(z=0.3$ m$)$ which are larger for

higher $T_{g,in}$. The temperature of the droplets approaches the temperature of the surrounding air at an axial distance $z=1.2$ m. The $\Delta T = T_g - T_{drop}$ increases when using a higher $T_{g,in}$ thus there is more capacity for evaporation when $T_{g,in}=473$ K than for $T_{g,in}=393$ K.

5.2.3. Inlet gas moisture content

Figure 8 shows temperature of the gas T_g, moisture content of the gas w_g, average temperature of the droplet T_{drop} and evaporated volume of vapor from the droplets to the air per unit time in the radial directions for three different values of inlet air moisture content. When w_g is low, more evaporation takes place without saturating the surrounding air. In the extreme case, when the humidity of the air is high ($w_{g,in}=0.1$ kg/kg), the water transfer from the droplet phase to the air is moderate. When the droplet evaporation rate is low, the temperature of the droplets approaches the temperature of the surrounding air.
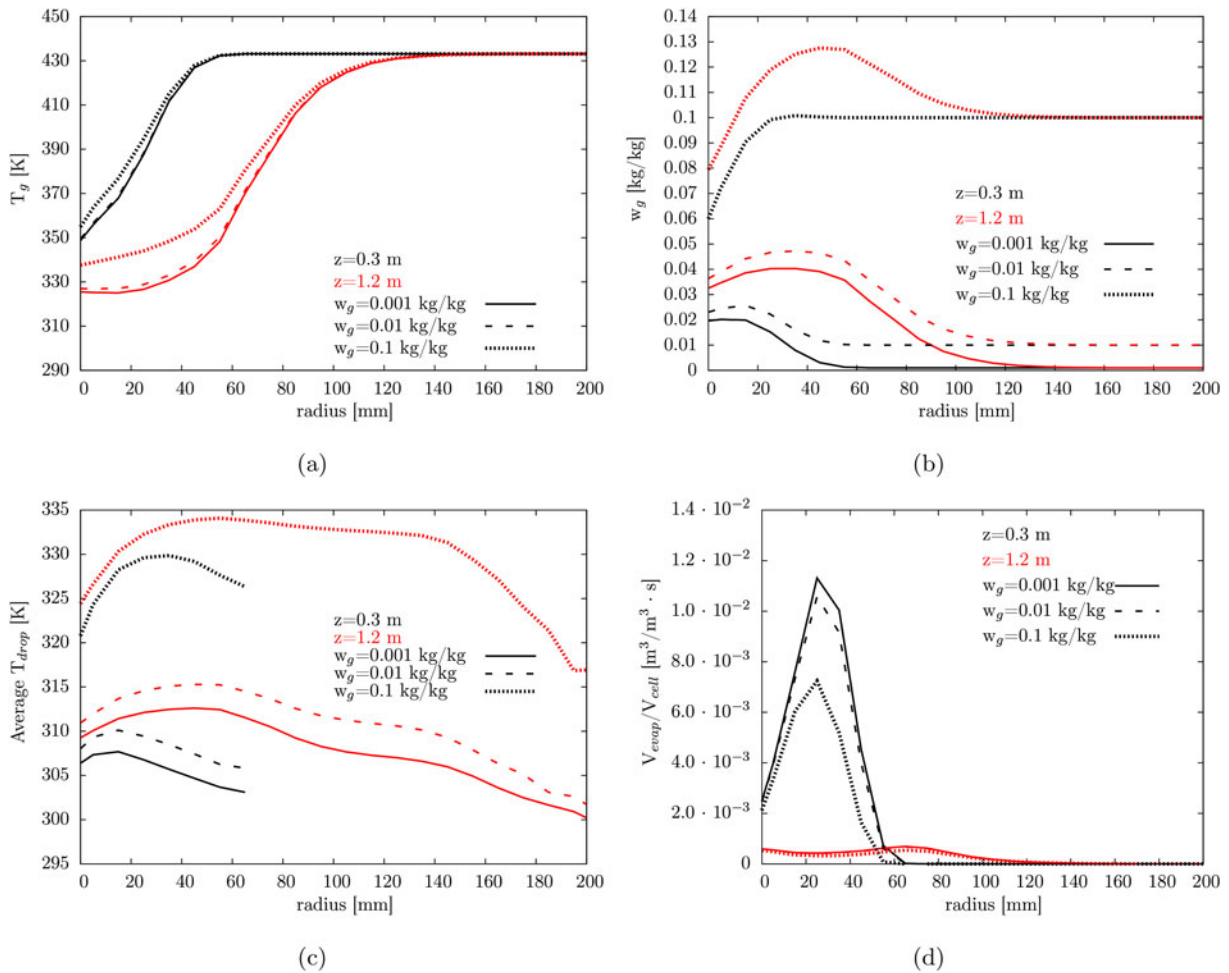
Figure 8. Temperature of the gas T_g (a), moisture content of the gas w_g (b), average temperature of the droplet T_{drop} (c) and normalized evaporated volume from the droplet phase to the air phase V_{evap}/V_{cell} per unit time (d) in the radial direction at two axial distances from the nozzle and for different inlet air moisture.
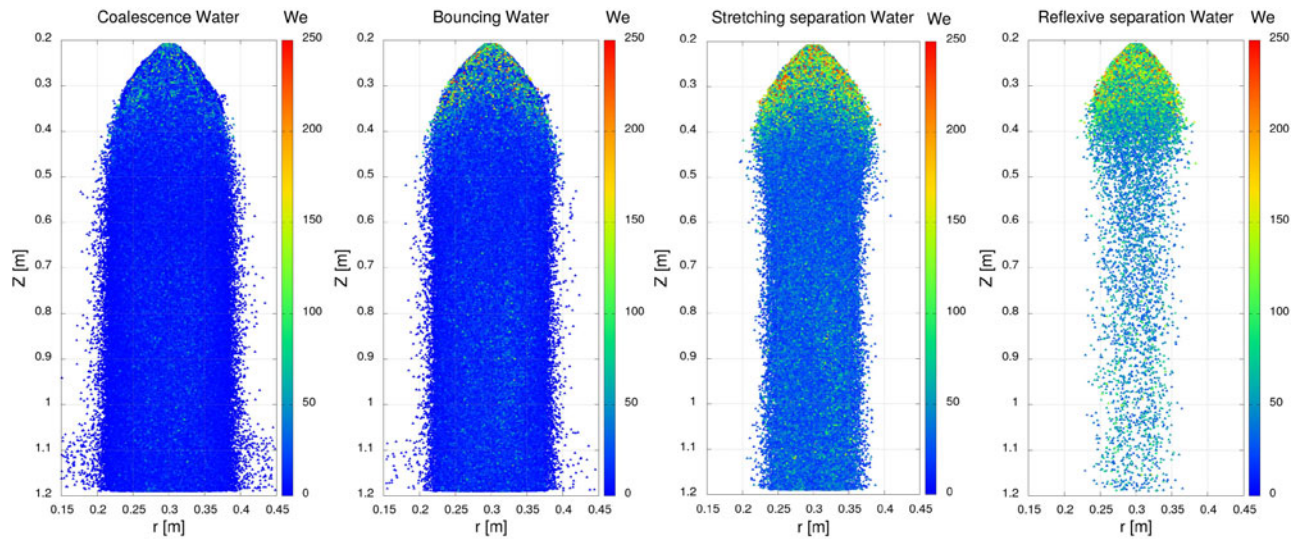

Figure 9. We number of the droplets in the entire spray system for coalescence, bouncing, stretching separation and reflexive separation for simulation **A**.

For $w_{g,in}=0.1$ kg/kg the air is close to saturation so that there is a local equilibrium between evaporation of the droplets and condensation of the water content of the air onto the droplets.
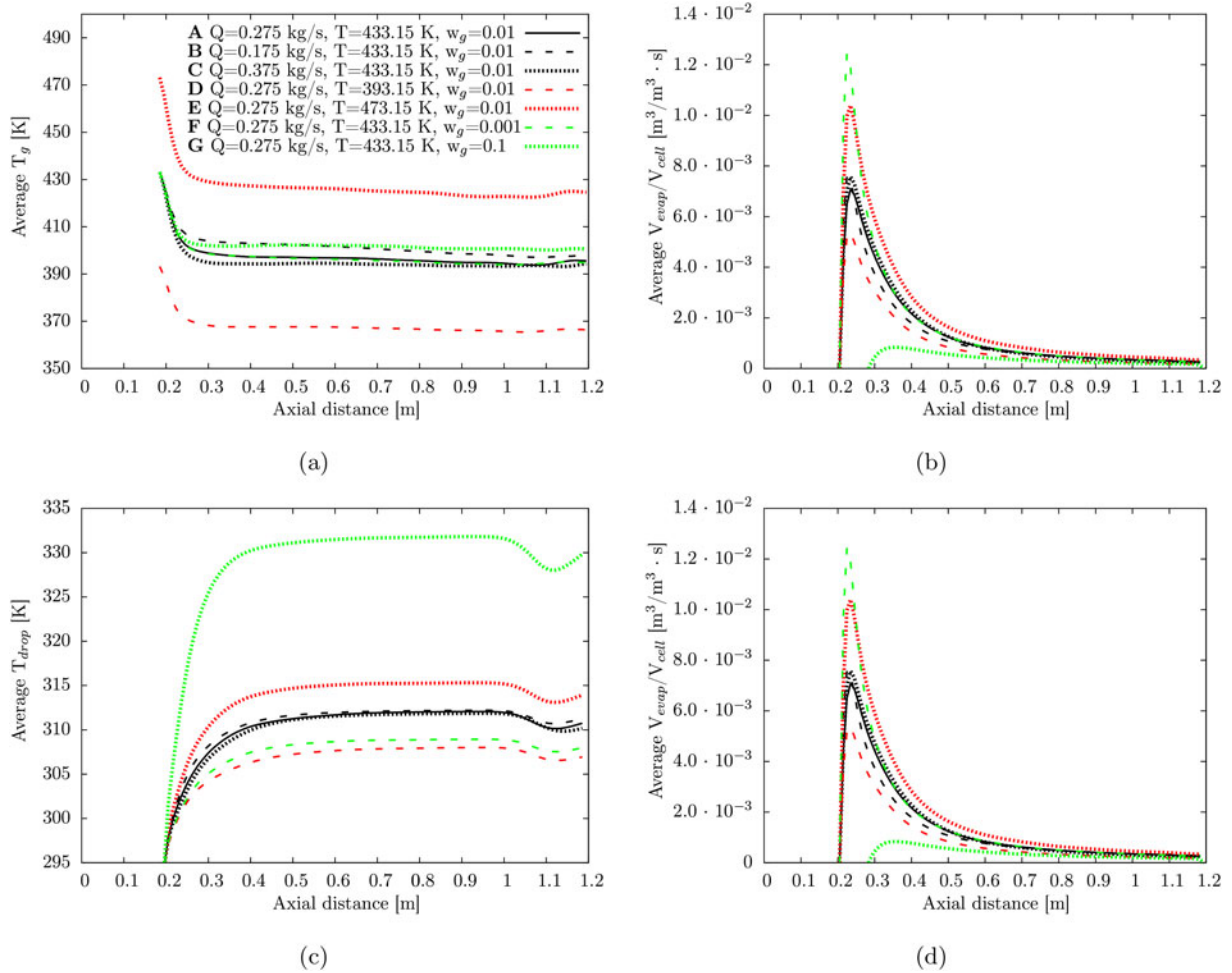
Figure 10. Temperature of the gas T_g (a), moisture content of the gas w_g (b), average temperature of the droplet T_{drop} (c) and normalized evaporated volume from the droplet phase to the air phase V_{evap}/V_{cell} per unit time (d) as a function of axial distance from the nozzle, for different inlet conditions. The legend of (a) is valid also for (b), (c) and (d).
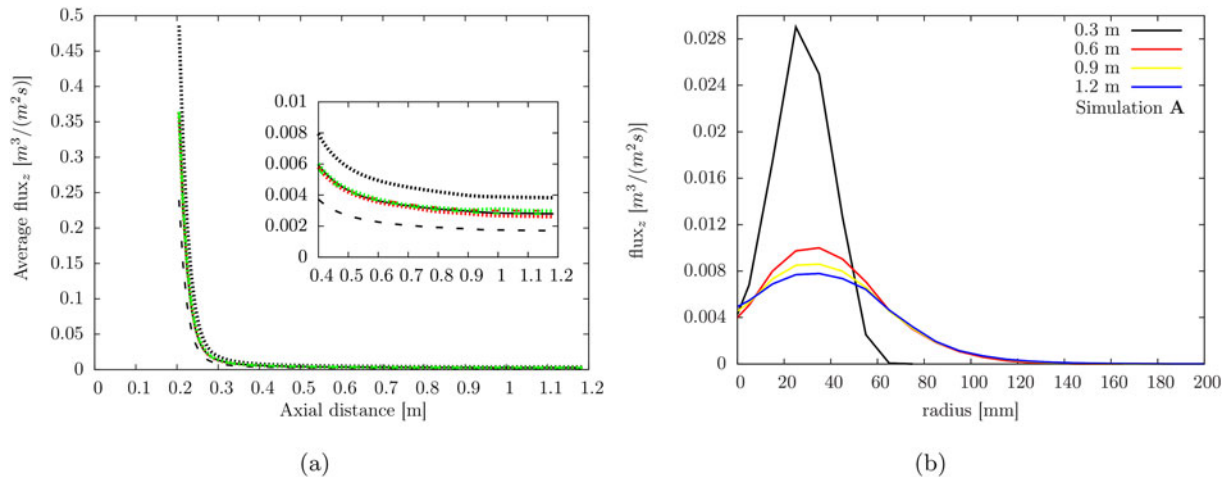

Figure 11. (a) droplet axial flux at different axial distances from the nozzle for all the simulations of the systematic study (for legend see Figure 10(a)); (b) droplet axial flux of simulation **A** as a function of lateral coordinate for four axial locations.

5.2.4. Axial profiles

Figure 10 shows the laterally averaged profiles of the air temperature T_g, air moisture content w_g, average temperature of the droplet T_{drop} and evaporated volume of vapor from the droplets to the air per unit time as a function of the axial coordinate. The largest

flow patterns changes occur in the proximity of the droplets inlet because of the high relative velocities between the air and the droplets coupled with large temperature and low humidity driving forces. This leads to very high heat and mass transfer rates. Most of the drying occurs in the first 10–20 cm while at larger axial distances the temperature and humidity change more slowly. This behavior is strongly related to the droplet flux along the spray. In the first 10-20 cm the large evaporation rate is caused by high slip velocities and large temperature and humidity gradients. Moreover the volume fraction of the droplets is largest in this region of the spray causing the highest evaporated mass per mass of air.

Figure 11(a) illustrates the droplet axial flux at different axial distances from the nozzle for all the simulations of the systematic study and Figure 11(b) shows the droplet axial flux of simulation **A** as a function of the lateral coordinate for three axial locations. The intensity of the transport phenomena close to the inlet can be attributed to the larger droplet flux. The liquid flux profiles in the lateral direction show the hollow cone nature of the initial configuration.

The average T_{drop} decrease, visible in Figure 10(c) at axial distance of 1 m, and subsequent increase might be related to a sudden variation of the droplet size distribution. Figure 12 shows that the larger droplets are at the bottom and towards the edges of the spray. But at larger axial distances the spray becomes also wider and few droplets are found beyond a lateral distances of 100 mm from the central axis. The size distribution at a lateral distance of r = 150 mm, see
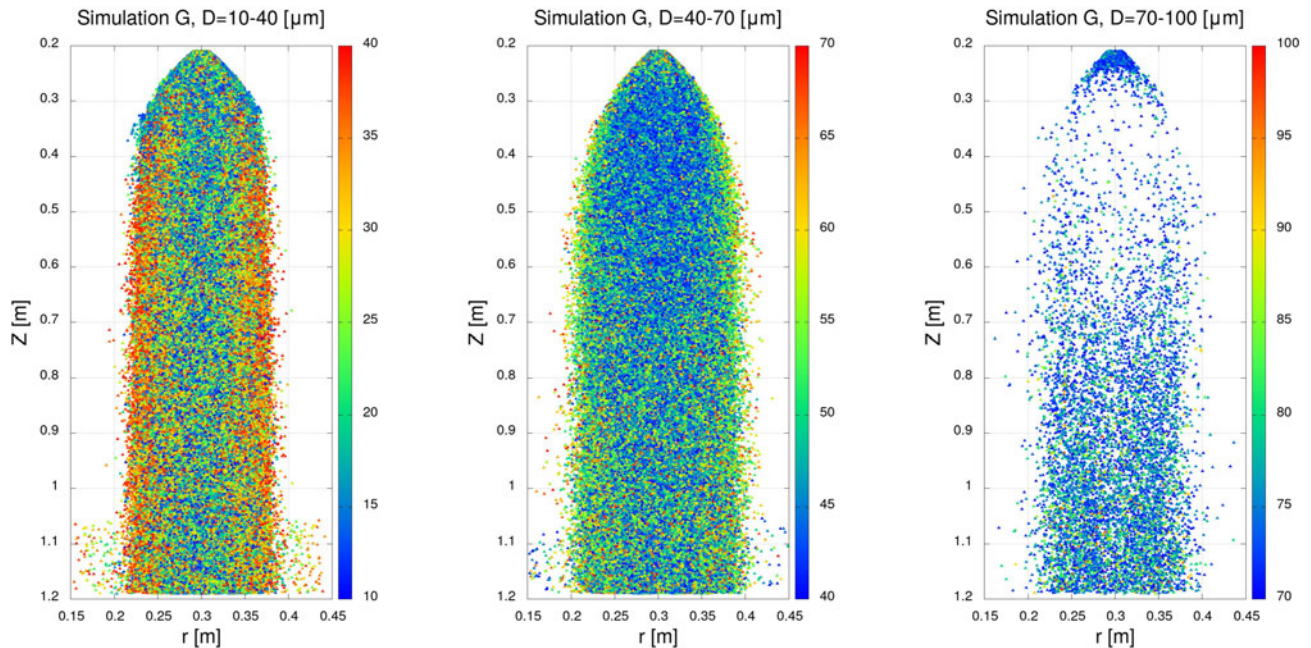

Figure 12. Diameters of the droplets in the entire spray system for coalescence for simulation **G**.
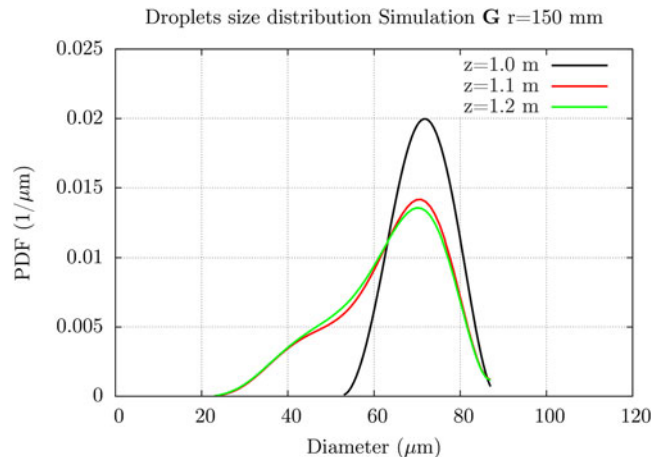

Figure 13. Droplet distribution function for the spray of simulation **G** at the three large axial distances.

Table 6. Number of collision outcomes until $t = 0.3$ s for the liquids considered in this work.

Liquids	Coalescence	Stretching separation	Reflexive separation	Bouncing	Total number of collisions ($\times \cdot 10^6$)
Water without drying and without coupling	31%	32.7%	0.7%	35.6%	11.8
Water with drying and without coupling	31%	33.3%	0.7%	35%	11.4
Water with drying and with coupling	30.9%	32.9%	0.7%	35.5%	11.7
Water **A**	30.9%	33.2%	0.7%	35.2%	11.5
Water **B**	33.2%	31.9%	0.6%	34.3%	5.6
Water **C**	29.1%	34.8%	0.7%	35.4%	18.7
Water **D**	31%	33%	0.7%	35.3%	11.6
Water **E**	30.9%	33.3%	0.7%	35.1%	11.3
Water **F**	30.9%	33.2%	0.7%	35.2%	11.4
Water **G**	31%	33%	0.8%	35.2%	11.7
Milk 20% TS	35.8%	63.5%	0.7%	–	11.4
Milk 46% TS	39.2%	60.7%	0.1%	–	10.5
Reference fluid	54.8%	45.2%	–	–	9.3

Figure 13, shifts to lower diameter when the axial distance z is increased. The presence of large droplets at $z = 1$ m decreases the average T_{drop} until $z = 1.1$ m where the T_{drop} increases again because of the small droplets at r larger than 100 mm. Larger droplets loose water in a much longer time than smaller droplets. The temperature reached by a large drop is lower than the one of a small drop.

In general, the analysis of the figures proves that air temperature and humidity are the most decisive factors for the intensity of the drying process. From Equations (23) and (24) it is clear that other two important factors that influence the drying process are the size distribution of the droplets and the droplets residence time in the spray dryer. Because larger droplets are less susceptible to air entrainment (i.e. have a higher Stokes number), they retain their high inlet velocity longer than smaller droplets, and so they are characterized by shorter residence time. But most of the larger droplets are found at the bottom and at the edges of the spray where their velocities are lower than the inlet velocities so they might have longer residence time. The overall evaporation rates will be affected both by the relative abundance of droplets of a given size and by the difference in drying history for such a group because of different residence times.

In Table 6, the total number of collisions, separated by collision type, up to time $t = 0.3$ s is listed for all the simulations of this work. The total number of collisions slightly reduces when drying is applied because of evaporation and consequent formation of smaller droplets. When droplet and air heat and mass transfer are coupled, the drying is less effective and the rate of collisions increases again. While for the drying rates the air temperature and humidity are the most influencial parameters, for the number of collisions the liquid flow rate is the most important parameter. This is obviously explained by the higher or lower number of droplets introduced when the flow rate is respectively higher or lower.

5.3. Effect of viscosity

The spray drying of droplets with solids content is described by two stages. When the droplet is in contact with the hot air, the air temperature drops rapidly because of the absorption of latent heat for the evaporation of water. During this stage the rate of moisture loss is constant and is compensated by moisture diffusion from the interior of the drop to the surface. Therefore the temperature of the droplet remains close to the wet bulb temperature of the air. In the second stage the moisture diffusion from the interior to the surface is less than the rate of moisture evaporation, so that the temperature of the droplet increases above the wet bulb temperature. The surface water concentration decreases, thus the evaporation rate decreases and the droplet temperature increases till approaching the air temperature.

Figure 14 shows the air temperature T_g (a), moisture content of the gas w_g (b), average temperature of the droplet T_{drop} (c) and average wet fraction of the droplets wt (d) as a function of the lateral coordinate at two axial distances from the nozzle and for different liquids. As expected for droplets with solid contents, the droplets reach a higher temperature when the viscosity increases because the rate of moisture evaporation is lower. For the gas phase a slight enlargement of the spray width is observed. The wet fraction profiles show that if the droplet at the inlet are more concentrated the drying is more intense because the difference of the average wet fraction from $z = 0.3$ m to $z = 1.2$ m is larger. Figure 15 shows the evaporation rate of the volume of moisture from the droplets, normalized by the droplet volume $\frac{1}{V_{drop}} \frac{dV_{evap}}{dt}$, averaged over the lateral direction per unit time as a function of the axial position. The
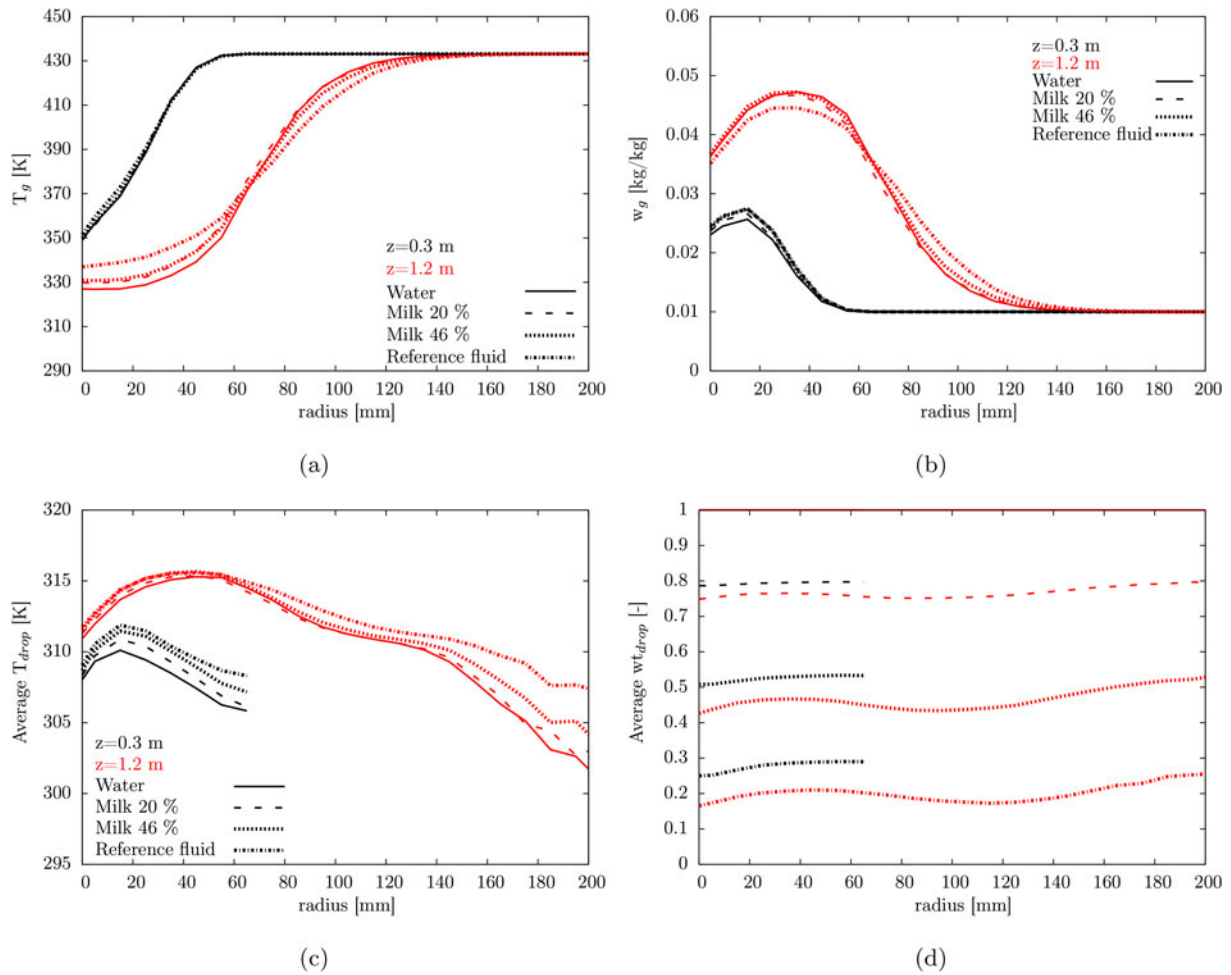
Figure 14. Temperature of the gas T_g (a), moisture content of the gas w_g (b), average temperature of the droplet T_{drop} (c) and average wet fraction of the droplets wt (d) in the lateral direction at two axial distances from the nozzle and for different liquids.
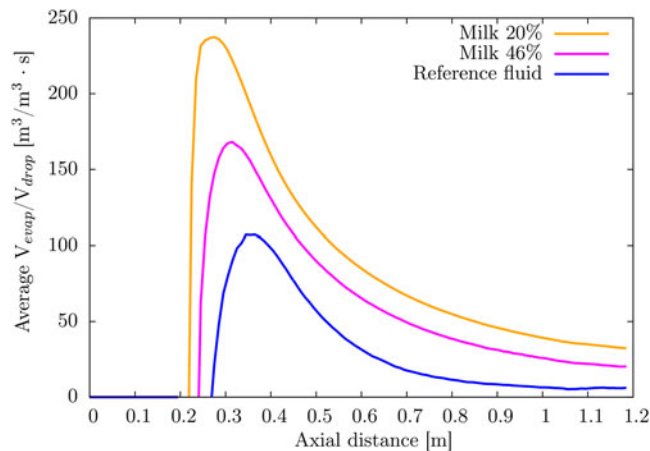

Figure 15. Normalized droplet evaporation rate $\frac{1}{V_{drop}}\frac{dV_{evap}}{dt}$ averaged over the lateral direction per unit time as a function of the axial position.

evaporated fraction is larger for liquids with lower solids content in the first 10–20 cm of the spray but it decreases more rapidly at larger axial distances.

A large droplet size and a short residence time in the spray chamber might result in a higher moisture content of the produced powder. Increased moisture content will weaken the flow properties, the bulk density and the stability of the powder.

The total number of collisions and the relative rates of collisions for the different regimes change drastically
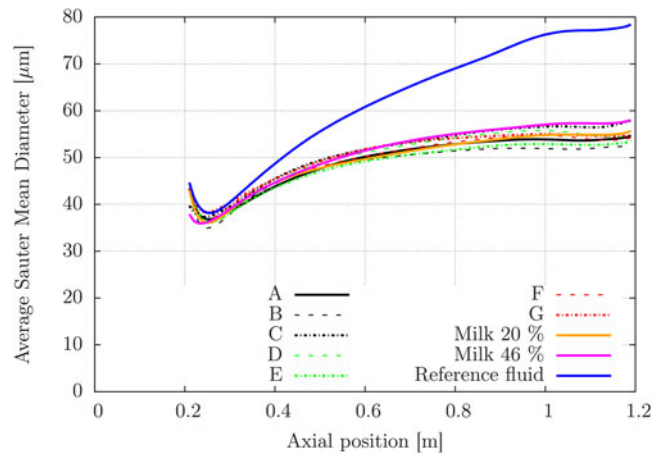
Figure 16. Sauter Mean Diameter averaged over the lateral direction as a function of the axial position for all the simulations of this work.

when milk concentrates are used. Finotello et al.[25] showed that separation and coalescence occur instead of bouncing for droplet collisions of whole milk. Moreover the frequency of coalescence increases when the droplet viscosity is higher. The same behavior is also observed in Table 6 for the spray of milk 20%, milk 46% and a reference fluid at very high viscosity.

We already observed in the case of a water spray as the droplet size distributions are not significantly affected by the process of evaporation and coupling with the air phase. The variation of inlet conditions such as those ones used in the parametric study are also not leading to a strong variation of the Sauter Mean Diameter, as shown in Figure 16. The increase in the Sauter Mean Diameter is instead due to the predominance of coalescence on separation events when the droplet viscosity is increased.

6. Conclusions

In this work, a spray dryer model has been developed by involving the heat and mass transfer balances for the gas phase and coupling the air with the droplet phase.

The droplet size distribution of the simulation with drying, heat and mass transfer produces smaller diameters on average than the simulation without drying and coupling because of the evaporation of water from the droplets.

From a systematic study of the effect of inlet conditions on the spray dryer, it was observed that near the central axis of the spray, there is less heat and mass transfer than at higher lateral positions. In fact, in the core of the spray, the liquid fraction is low. In the axial direction, most of the heat and mass transfer occurs in the first few centimeters because of the high

air to droplet velocity differences coupled with high temperature and mass transfer driving forces. With increasing axial distance the droplet temperature increases, but does not reach the temperature of the gas phase. Most of the heat from the gas phase is used for evaporation. Despite the evaporation, the diameter of the droplets increases, both in the axial and lateral direction, because of coalescence collisional events, which occur in the whole droplet spray.

In the current model the milk droplets are simplified as consisting of liquid only without considering sticking particles agglomeration. This is a main subject for future work to get deeper insight into the spray dryer process performance in term of energy and quality of the product. In this work the effect of viscosity was investigated through its effect on the outcome of droplet-droplet collisions. The predicted droplet temperature is higher for higher solids content. The droplet spray of milk is slightly wider than the droplet spray of water. The effect of drying with increase of the droplet temperature at higher viscosities is moderated by higher frequency of coalescence.

The amount of water that has evaporated at the bottom of the spray dryer is relatively small for the considered operating conditions and also the relative humidity of the air phase is still very low. To study a full spray dryer performance, the domain size should be increased or the atomization should produce smaller drops or recirculation of fines should be adopted.

Nomenclature

A_i	Droplet surface area m^2
a_i	Specific fluid-droplet surface area m^2
C_p	Specific heat capacity J/(kg · K)
d_i	Droplet diameter m
d_s	Droplet diameter of the smallest droplet m
d_l	Droplet diameter of the largest droplet m

$D_{e,g}$	Gas diffusion coefficient m^2/s
$D_{eff,g}$	Effective gas diffusivity m^2/s
$f(Re)$	Drag factor –
f_i	Collision frequency of droplet i $1/s$
$H_{f,g}$	Specific latent heat of evaporation J/kg
h_g	Convective heat transfer coefficient of the gas W/(m$^2 \cdot$ K)
H_g	Enthalpy of the gas J/kg
k	Kinetic energy per unit mass J/kg
k_{eff}	Effective thermal conductivity W/(m $\cdot$ K)
k_g	Thermal conductivity W/(m $\cdot$ K)
k_m	Mass transfer coefficient m/s
L_i	mean free path of droplet i m
$\dot{m}_i$	Rate of moisture evaporation kg/s
m_i	Droplet mass kg
M_{air}	Molecular weight of air kg/mol
M_d	Molecular weight of the droplet liquid kg/mol
N_i	Number of droplets in the searching scope of i
n_j	Number of real droplets represented by j
P	Gas pressure Pa
P_v^*	Partial vapor pressure Pa
$P_{v,sat}^*$	Saturation partial vapor pressure Pa
$P_{i,j}$	Collision probability between droplet i and j
$\mathbf{q}_h$	Conductive heat flux W/m^2
$\mathbf{q}_m$	Mass transfer flux m/s
R	Gas constant J/(mol $\cdot$ K)
$R_{s,i}$	Collision searching scope of droplet i m
$\mathbf{r}$	Grid position
$\mathbf{r}_i$	Droplet position
RH_g	Gas relative humidity
S_p	Source term for drag force N/m^3
S_h	Source term for heat transfer W/m^3
S_m	Source term for mass transfer kg/(m$^3 \cdot$ s)
T_∞	Fluid bulk temperature K
T_i	Droplet temperature K
T_g	Gas temperature K
T_{in}	Inlet temperature K
T_{ref}	Reference temperature K
$\mathbf{u}_g$	Gas velocity m/s
u_{sgs}	Subgrid velocity m/s
$\mathbf{u}_{rel}$	Relative velocity between gas-droplet m/s
$\mathbf{u}_i^*$	Stochastic subgrid velocity at the location of the droplet m/s
$\mathbf{v}_i$	Droplet velocity m/s
v_{ij}	Relative velocity between droplet i and j m/s
V_i	Droplet volume m^3
V_{cell}	Cell volume m^3
w_g	Mass fraction of moisture in the gas phase kg/kg
w_g^*	Saturated concentration of liquid at the solid liquid interface kg/kg
X_g	Equilibrium moisture content in the bulk of air phase kg/kg
X_i	Wet fraction kg/kg

Greek symbols

α	Thermal diffusivity m^2/s
β	Inter-phase momentum transfer coefficient kg/(m$^3 \cdot$ s)
δ	Discrete delta function
ε	Porosity
ζ	random vector

ϑ	Normalized drift velocity
μ_g	Viscosity of the gas kg/(m $\cdot$ s)
μ_d	Viscosity of the droplet kg/(m $\cdot$ s)
ρ_d	Droplet density kg/m^3
ρ_g	Gas density kg/m^3
σ	Surface tension N/m
$\bar{\tau}_g$	Stress tensor Pa
τ_d	Droplet dynamic relaxation time s
τ_L^*	Lagrangian time s
τ_{sgs}	Subgrid scale time s
ΔE_v	Apparent activation energy J/mol
$\Delta t_{d,i}$	Time step for droplet i s
Δt_g	Gas time step s
Ψ	Fractionality

Dimensionless numbers

Nu	Nusselt number	$Nu = \frac{h_g d_d}{k_g}$
Pr	Prandtl number	$Pr = \frac{\mu_g C_{p,g}}{k_g}$
Re	Reynolds number	$Re = \frac{\varepsilon \rho_g |\mathbf{u}_g - \mathbf{v}_d| d_d}{\mu_g}$
Sc	Schmidt number	$Sc = \frac{\mu_g}{\rho_g D_{e,g}}$
Sh	Sherwood number	$Sh = \frac{k_m d_d}{D_{e,g}}$
We	Weber number	$We = \frac{\rho_d d_s |v_{ij}|^2}{\sigma}$
Oh	Ohnesorge number	$Oh = \frac{\mu_d}{\sqrt{\rho_d d_s \sigma}}$
B	Impact parameter	$B = \frac{2b}{d_s + d_l}$

Funding

References

[1] Baker, C. Energy Efficient Dryer Operation—An Update on Developments. *Drying Technol.* **2005**, *23*, 2071–2087. DOI: 10.1080/07373930500210556.

[2] Goula, A. M.; Adamopoulos, K. G. Spray Drying Performance of a Laboratory Spray Dryer for Tomato Powder Preparation. *Drying Technol.* **2003**, *21*, 1273–1289. DOI: 10.1081/DRT-120023180.

[3] Kim, E. H. J.; Chen, X. D.; Pearce, D. Surface Composition of Industrial Spray-Dried Milk Powders. 2. Effects of Spray Drying Conditions on the Surface Composition. *J. Food Eng.* **2009**, *94*, 169–181. DOI: 10.1016/j.jfoodeng.2008.10.020.

[4] Dlouhy, J.; Gauvin, W. Heat and Mass Transfer in Spray Drying. *AIChE J.* **1960**, *6*, 29–34. DOI: 10.1002/aic.690060106.

[5] Fletcher, D.; Guo, B.; Harvie, D.; Langrish, T.; Nijdam, J.; Williams, J. What is Important in the Simulation of Spray Dryer Performance and How Do Current CFD Models Perform? *Appl. Math. Model.* **2006**, *30*, 1281–1292. DOI: 10.1016/j.apm.2006.03.006.

[6] Langrish, T.; Fletcher, D. Prospects for the Modelling and Design of Spray Dryers in the 21st Century. *Drying Technol.* **2003**, *21*, 197–215. DOI: 10.1081/DRT-120017743.

[7] Kuriakose, R.; Anandharamakrishnan, C. Computational Fluid Dynamics (CFD) Applications in Spray Drying of Food Products. *Trends Food Sci Technol.* **2010**, *21*, 383–398. DOI: 10.1016/j.tifs.2010.04.009.

[8] Zbicinski, I.; Grabowski, S.; Strumillo, C.; Kiraly, L.; Krzanowski, W. Mathematical Modelling of Spray Drying. *Comput. Chem. Eng.* **1988**, *12*, 209–214. DOI: 10.1016/0098-1354(88)85029-4.

[9] Langrish, T. Multi-Scale Mathematical Modelling of Spray Dryers. *J. Food Eng.* **2009**, *93*, 218–228. DOI: 10.1016/j.jfoodeng.2009.01.019.

[10] Li, X.; Zbiciński, I. A Sensitivity Study on CFD Modeling of Cocurrent Spray-Drying Process. *Drying Technol.* **2005**, *23*, 1681–1691. DOI: 10.1081/DRT-200065093.

[11] Zbiciński, I.; Li, X. Conditions for Accurate CFD Modeling of Spray-Drying Process. *Drying Technol.* **2006**, *24*, 1109–1114. DOI: 10.1080/07373930600778221.

[12] Chen, X.; Pirini, W.; Ozilgen, M. The Reaction Engineering Approach to Modelling Drying of Thin Layer of Pulped Kiwifruit Flesh under Conditions of Small Biot Numbers. *Chem. Eng. Process Process Intensification* **2001**, *40*, 311–320. DOI: 10.1016/S0255-2701(01)00108-8.

[13] Chen, X. D.; Putranto, A. *Modelling Drying Processes: A Reaction Engineering Approach.* Cambridge University Press: Cambridge, **2013**.

[14] Chen, X. D.; Lin, S. X. Q. Air Drying of Milk Droplet under Constant and Time-Dependent Conditions. *AIChE J.* **2005**, *51*, 1790–1799. DOI: 10.1002/aic.10449.

[15] Qi Lin, S. X.; Chen, X. D. Prediction of Air-Drying of Milk Droplet under Relatively High Humidity Using the Reaction Engineering Approach. *Drying Technol.* **2005**, *23*, 1395–1406. DOI: 10.1081/DRT-200063486.

[16] Patel, K. C.; Chen, X. D. Sensitivity Analysis of the Reaction Engineering Approach to Modeling Spray Drying of Whey Proteins Concentrate. *Drying Technol.* **2008**, *26*, 1334–1343. DOI: 10.1080/07373930802331019.

[17] Lin, S. X. Q.; Chen, X. D. A Model for Drying of an Aqueous Lactose Droplet Using the Reaction Engineering Approach. *Drying Technol.* **2006**, *24*, 1329–1334. DOI: 10.1080/07373930600951091.

[18] Huang, L.; Kumar, K.; Mujumdar, A. A Parametric Study of the Gas Flow Patterns and Drying Performance of co-Current Spray Dryer: Results of a Computational Fluid Dynamics Study. *Drying Technol.* **2003**, *21*, 957–978. DOI: 10.1081/DRT-120021850.

[19] Kieviet, F.; Kerkhof, P. Air Flow, Temperature and Humidity Patterns in a co-Current Spray Dryer: Modelling and Measurements. *Drying Technol.* **1997**, *15*, 1763–1773. DOI: 10.1080/07373939708917325.

[20] Kieviet, F. G. *Modeling Quality in Spray Drying. Doctor of Philosophy.* Eindhoven University of Technology: The Netherlands, **1997**.

[21] Mezhericher, M.; Levy, A.; Borde, I. Droplet–Droplet Interactions in Spray Drying by Using 2d Computational Fluid Dynamics. *Drying Technol.* **2008**, *26*, 265–282. DOI: 10.1080/07373930801897523.

[22] Finotello, G.; Padding, J.; Buist, K.; Jongsma, A.; Innings, F.; Kuipers, J. A. M. Droplet Collisions of Water and Milk in a Spray with Langevin Turbulence Dispersion. *Int. J. Multiphase Flow* **2019**, *114*, 154–167.

[23] Ashgriz, N.; Poo, J. Coalescence and Separation in Binary Collisions of Liquid Drops. *J. Fluid Mech.* **1990**, *221*, 183–204. DOI: 10.1017/S0022112090003536.

[24] Jiang, Y.; Umemura, A.; Law, C. An Experimental Investigation on the Collision Behaviour of Hydrocarbon Droplets. *J. Fluid Mech.* **1992**, *234*, 171–190. DOI: 10.1017/S0022112092000740.

[25] Finotello, G.; Kooiman, R.; Padding, J.; Buist, K.; Jongsma, A.; Innings, F.; Kuipers, J. A. M. The Dynamics of Milk Droplet-Droplet Collisions. *Exp. Fluids* **2018**, *59*, 17. DOI: 10.1007/s00348-017-2471-2.

[26] Qian, J.; Law, C. Regimes of Coalescence and Separation in Droplet Collision. *J. Fluid Mech.* **1997**, *331*, 59–80. DOI: 10.1017/S0022112096003722.

[27] Brenn, G.; Kolobaric, V. Satellite Droplet Formation by Unstable Binary Drop Collisions. *Phys. Fluids (1994-Present)* **2006**, *18*, 087101. DOI: 10.1063/1.2225363.

[28] Ko, G. H.; Ryou, H. S. Modeling of Droplet Collision-Induced Breakup Process. *Int. J. Multiphase Flow* **2005**, *31*, 723–738. DOI: 10.1016/j.ijmultiphaseflow.2005.02.004.

[29] Gotaas, C.; Havelka, P.; Jakobsen, H. A.; Svendsen, H. F.; Hase, M.; Roth, N.; Weigand, B. Effect of Viscosity on Droplet-Droplet Collision Outcome: Experimental Study and Numerical Comparison. *Phys. Fluids (1994-Present)* **2007**, *19*, 102106. DOI: 10.1063/1.2781603.

[30] Kuschel, M.; Sommerfeld, M. Investigation of Droplet Collisions for Solutions with Different Solids Content. *Exp. Fluids* **2013**, *54*, 1–17. DOI: 10.1007/s00348-012-1440-z.

[31] Sommerfeld, M.; Kuschel, M. Modelling Droplet Collision Outcomes for Different Substances and Viscosities. *Exp. Fluids* **2016**, *57*, 187. DOI: 10.1007/s00348-016-2249-y.

[32] Pan, Y.; Suga, K. Numerical Simulation of Binary Liquid Droplet Collision. *Phys. Fluids (1994-Present)* **2005**, *17*, 082105. DOI: 10.1063/1.2009527.

[33] Munnannur, A.; Reitz, R. D. A New Predictive Model for Fragmenting and Non-Fragmenting Binary Droplet Collisions. *Int. J. Multiphase Flow* **2007**, *33*, 873–896. DOI: 10.1016/j.ijmultiphaseflow.2007.03.003.

[34] Nikolopoulos, N.; Nikas, K. S.; Bergeles, G. A Numerical Investigation of Central Binary Collision of Droplets. *Comput. Fluids* **2009**, *38*, 1191–1202. DOI: 10.1016/j.compfluid.2008.11.007.

[35] Focke, C.; Bothe, D. Computational Analysis of Binary Collisions of Shear-Thinning Droplets. *J Non-Newtonian Fluid Mech.* **2011**, *166*, 799–810. DOI: 10.1016/j.jnnfm.2011.03.011.

[36] Focke, C.; Bothe, D. Direct Numerical Simulation of Binary off-Center Collisions of Shear Thinning

Droplets at High Weber Numbers. *Phys. Fluids* **2012**, *24*, 073105–073180. DOI: 10.1063/1.4737582.

[37] Sun, K.; Zhang, P.; Law, C. K.; Wang, T. Collision Dynamics and Internal Mixing of Droplets of Non-Newtonian Liquids. *Phys. Rev. Appl.* **2015**, *4*, 054013. DOI: 10.1103/PhysRevApplied.4.054013.

[38] Finotello, G.; De, S.; Vrouwenvelder, J. C. R.; Padding, J. T.; Buist, K. A.; Jongsma, A.; Innings, F.; Kuipers, J. A. M. Experimental Investigation of Non-Newtonian Droplet Collisions: The Role of Extensional Viscosity. *Exp. Fluids* **2018**, *59*, 113. DOI: 10.1007/s00348-018-2568-2.

[39] Sommerfeld, M.; Qiu, H. H. Experimental Studies of Spray Evaporation in Turbulent Flow. *Int. J. Heat Fluid Flow* **1998**, *19*, 10–22. DOI: 10.1016/S0142-727X(97)10002-9.

[40] Birchal, V.; Huang, L.; Mujumdar, A.; Passos, M. Spray Dryers: Modeling and Simulation. *Drying Technol.* **2006**, *24*, 359–371. DOI: 10.1080/07373930600564431.

[41] Gianfrancesco, A.; Turchiuli, C.; Dumoulin, E. Powder Agglomeration during the Spray-Drying Process: Measurements of Air Properties. *Dairy Sci. Technol.* **2008**, *88*, 53–64. DOI: 10.1051/dst:2007008.

[42] Gimbun, J.; Law, W.; Anandharamakrishnan, C. Computational Fluid Dynamics Modelling of the Dairy Drying Processes. In *Handbook of Drying for Dairy Products*, Anandharamakrishnan, C., Ed.; John Wiley & Sons, **2017**; pp 179–201.

[43] Pawar, S. K.; Padding, J. T.; Deen, N. G.; Jongsma, A.; Innings, F.; Kuipers, J. A. M. Lagrangian Modelling of Dilute Granular Flow-Modified Stochastic DSMC versus Deterministic DPM. *Chem. Eng. Sci.* **2014**, *105*, 132–142. DOI: 10.1016/j.ces.2013.11.004.

[44] Pawar, S. K.; Padding, J. T.; Deen, N. G.; Jongsma, A.; Innings, F.; Kuipers, J. A. M. Numerical and Experimental Investigation of Induced Flow and Droplet–Droplet Interactions in a Liquid Spray. *Chem. Eng. Sci.* **2015**, *138*, 17–30. DOI: 10.1016/j.ces.2015.07.048.

[45] Sutkar, V.; Deen, N.; Patil, A.; Salikov, V.; Antonyuk, S.; Heinrich, S.; Kuipers, J. A. M. CFD–DEM Model for Coupled Heat and Mass Transfer in a Spout Fluidized Bed with Liquid Injection. *Chem. Eng. J.* **2016**, *288*, 185–197. DOI: 10.1016/j.cej.2015.11.044.

[46] Van Buijtenen, M. S.; Deen, N. G.; Heinrich, S.; Antonyuk, S.; Kuipers, J. A. M. A Discrete Element Study of Wet Particle–Particle Interaction during Granulation in a Spout Fluidized Bed. *Can. J. Chem. Eng.* **2009**, *87*, 308–317. DOI: 10.1002/cjce.20144.

[47] Beetstra, R.; van der Hoef, M. A.; Kuipers, J. A. M. Drag Force of Intermediate Reynolds Number Flow past Mono-and Bidisperse Arrays of Spheres. *AIChE J.* **2007**, *53*, 489–501. DOI: 10.1002/aic.11065.

[48] Vreman, A. An Eddy-Viscosity Subgrid-Scale Model for Turbulent Shear Flow: Algebraic Theory and Applications. *Phys. Fluids (1994-Present)* **2004**, *16*, 3670–3681. DOI: 10.1063/1.1785131.

[49] Irannejad, A.; Jaberi, F. Large Eddy Simulation of Turbulent Spray Breakup and Evaporation. *Int. J. Multiphase Flow* **2014**, *61*, 108–128. DOI: 10.1016/j.ijmultiphaseflow.2014.01.004.

[50] Sommerfeld, M. Validation of a Stochastic Lagrangian Modelling Approach for Inter-Particle Collisions in Homogeneous Isotropic Turbulence. *Int. J. Multiphase Flow* **2001**, *27*, 1829–1858. DOI: 10.1016/S0301-9322(01)00035-0.

[51] Ranz, W.; Marshall, W. R. Evaporation from Drops. *Chem. Eng. Prog.* **1952**, *48*, 141–146.

[52] Pozorski, J.; Apte, S. V. Filtered Particle Tracking in Isotropic Turbulence and Stochastic Modeling of Subgrid-Scale Dispersion. *Int. J. Multiphase Flow* **2009**, *35*, 118–128. DOI: 10.1016/j.ijmultiphaseflow.2008.10.005.

[53] Estrade, J. P.; Carentz, H.; Lavergne, G.; Biscos, Y. Experimental Investigation of Dynamic Binary Collision of Ethanol Droplets–A Model for Droplet Coalescence and Bouncing. *Int. J. Heat Fluid Flow* **1999**, *20*, 486–491. DOI: 10.1016/S0142-727X(99)00036-3.

[54] Verdurmen, R.; van Houwelingen, G.; Gunsing, M.; Verschueren, M.; Straatsma, J. Agglomeration in Spray Drying Installations (The Edecad Project): Stickiness Measurements and Simulation Results. *Drying Technol.* **2006**, *24*, 721–726. DOI: 10.1080/07373930600684973.

[55] Sommerfeld, M.; Stübing, S. A Novel Lagrangian Agglomerate Structure Model. *Powder Technol.* **2017**, *319*, 34–52. DOI: 10.1016/j.powtec.2017.06.016.

[56] ASHRAE. *Handbook ASHRAE Fundamentals*. American Society of Heating, Refrigerating and Air Conditioning Engineers: Atlanta, **2001**; pp 111.